

# **UC Irvine**

## **UC Irvine Electronic Theses and Dissertations**

**Title**

Reduction of Tonal Propeller Noise by Means of Uneven Blade Spacing

**Permalink**

<https://escholarship.org/uc/item/9q75v9t9>

**Author**

Kim, Tae

**Publication Date**

2016

Peer reviewed|Thesis/dissertation

UNIVERSITY OF CALIFORNIA,  
IRVINE

Reduction of Tonal Propeller Noise by Means of Uneven Blade Spacing  
THESIS

submitted in partial satisfaction of the requirements  
for the degree of

MASTERS OF SCIENCE  
in Mechanical and Aerospace Engineering

by

Tae Young Kim

Thesis Committee:  
Professor Dimitri Papamoschou, Chair  
Professor Robert H. Liebeck  
Professor Feng Liu

2016

© 2016 Tae Young Kim

# TABLE OF CONTENTS

	Page
<b>LIST OF FIGURES</b>	<b>iv</b>
<b>LIST OF TABLES</b>	<b>vi</b>
<b>ACKNOWLEDGMENTS</b>	<b>vii</b>
<b>CURRICULUM VITAE</b>	<b>viii</b>
<b>ABSTRACT OF THE DISSERTATION</b>	<b>xi</b>
<b>1 Introduction</b>	<b>1</b>
1.1 Motivation . . . . .	1
1.2 Background . . . . .	1
1.2.1 Elements of Propeller Noise . . . . .	2
1.2.2 Previous Works . . . . .	3
1.3 Objectives . . . . .	4
1.4 Thesis Overview . . . . .	5
<b>2 Theoretical Work</b>	<b>6</b>
2.1 Noise Prediction of a Propeller with Even Blade Spacing . . . . .	6
2.2 Superposition of Propellers with Even Blade Spacing . . . . .	9
2.3 Results of Theoretical Analysis . . . . .	10
<b>3 Propeller Design</b>	<b>13</b>
3.1 McCauley Propeller . . . . .	13
3.2 Subscale Propellers . . . . .	14
<b>4 Experimental Details</b>	<b>19</b>
4.1 Power Plant . . . . .	19
4.2 Data Measurement and Collection . . . . .	20
4.2.1 Acoustic Pressure Measurement . . . . .	20
4.2.2 Thrust Measurement . . . . .	21
4.2.3 RPM Measurement . . . . .	22
4.3 Data Processing . . . . .	23
4.3.1 Sound Pressure Level . . . . .	23

4.3.2	Overall Sound Pressure Level . . . . .	24
<b>5</b>	<b>Results and Analysis</b>	<b>26</b>
5.1	Tip Mach Number and Disc Loading . . . . .	26
5.2	Power Spectra . . . . .	28
5.3	Overall Sound Pressure Level . . . . .	39
<b>6</b>	<b>Conclusion</b>	<b>43</b>
6.1	Summary . . . . .	43
6.2	Recommendations for future work . . . . .	44
	<b>Bibliography</b>	<b>45</b>
<b>A</b>	<b>Blade Element Momentum Theory</b>	<b>48</b>
<b>B</b>	<b>Stress Analysis</b>	<b>54</b>
<b>C</b>	<b>Unweighted vs. A-weighted Spectra</b>	<b>58</b>
<b>D</b>	<b>Unweighted Spectra</b>	<b>62</b>
<b>E</b>	<b>Unweighted Spectra, Compound Propellers</b>	<b>65</b>

# LIST OF FIGURES

	Page
1.1 Applications of uneven blade spacing found in the Nissan Sentra's radiator cooling fan (left) [22] and in the Eurocopter EC135 helicopter tail rotor (right), courtesy of Christoph Hansa. ( <a href="https://en.wikipedia.org/wiki/File:RTH_Christoph_Hansa_06.jpg">https://en.wikipedia.org/wiki/File:RTH_Christoph_Hansa_06.jpg</a> )	4
2.1 Distribution of monopole sources (blue dots) along the normalized chord X. H(X) represents the normalized thickness distribution.	8
2.2 Distribution of dipole sources (blue dots) along the normalized chord X. P(X) represents the normalized net pressure distribution acting on the blade section.	9
2.3 Acoustic phase shift validation	10
2.4 $\Delta$ OASPL(A) map	11
2.5 $\Delta$ OASPL(A) for $\epsilon = 15^\circ, 20^\circ, 25^\circ, 30^\circ$	12
3.1 The latest update to the 350 series, the Beechcraft King Air 350i [4].	14
3.2 Chord and thickness modifications.	15
3.3 Twist modification.	16
3.4 Airfoil profile modification.	17
3.5 3D drawings of propellers with separation angles: $90^\circ$ (top), $30^\circ$ (bottom left), $20^\circ$ (bottom right). Drawings were generated on Solidworks.	17
3.6 Printed propellers with separation angles: $90^\circ$ (left), $30^\circ$ (center), $20^\circ$ (right).	18
4.1 Electronics block diagram.	19
4.2 Anechoic chamber schematic.	20
4.3 Anechoic chamber setup with the $\epsilon 30$ propeller.	21
4.4 Motor support and thrust measurement assembly.	22
4.5 RPM sensor block diagram, designed by Truong [33].	23
4.6 A-weighting correction curve [2].	25
5.1 Comparison of thrust (left) and disc loading (right) between theory and experiments.	27
5.2 Spectra for $\epsilon 90$ (top), $\epsilon 30$ (middle), and $\epsilon 20$ (bottom) with labeled tones for downward noise at $\theta = 96.7^\circ$ .	29
5.3 Spectra showing the increases in broadband noise in $\epsilon 30$ (top) and $\epsilon 20$ (bottom) for downward noise at $\theta = 44.2^\circ$ .	30
5.4 Section view of propeller showing the merging of blades near the hub.	30
5.5 Compound propeller mounted onto motor for testing.	31
5.6 Compound propellers: $\epsilon 30$ (top) and $\epsilon 20$ (bottom) for downward noise at $\theta = 44.2^\circ$ .	31

5.7	Extraction of tonal noise from power spectrum. The fixed width of 120 hz translates into 4 data points for a 4096 point-Fourier transform. . . . .	32
5.8	Filtered spectra for downward noise at $\theta = 96.7^\circ$ . Extracted tones are shaded in red. The acoustic intensity for each tone is displayed above the tone in $\text{Pa}^2$ . . . . .	33
5.9	Tonal acoustic intensity for downward (left) and sideline (right) noise. . . . .	34
5.10	Percent difference in acoustic intensity from the $\varepsilon_{90}$ propeller. . . . .	34
5.11	Percent of total acoustic intensity contained in the 0.5BPF tone. . . . .	35
5.12	Total acoustic intensity without the 0.5BPF tone. . . . .	35
5.13	Changes in acoustic intensity in “regular tones.” . . . . .	37
5.14	Shifting of acoustic intensity into “new” tones. . . . .	38
5.15	Unweighted and A-weighted spectra of $\varepsilon_{90}$ (top), $\varepsilon_{30}$ (middle), and $\varepsilon_{20}$ (bottom) at $\theta = 96.7^\circ$ . A-weighting is performed after scaling the frequencies with the model scale factor. . . . .	39
5.16	OASPL(A) of 0.5BPF through 5BPF tones. . . . .	40
5.17	Change in OASPL(A) from the $\varepsilon_{90}$ propeller compared to theoretical predictions. .	40
5.18	OASPL(A) from the $\varepsilon_{90}$ propeller with the 5.5BPF tone. . . . .	41
5.19	Change in OASPL(A) from the $\varepsilon_{90}$ propeller with the 5.5BPF tone. . . . .	41
5.20	Changes in OASPL(A) from the $\varepsilon_{90}$ propeller with both tonal and broadband noise. .	42

## **LIST OF TABLES**

	Page
5.1 RPM, tip Mach number, and disc loading. . . . .	27

## **ACKNOWLEDGMENTS**

First and foremost, I would like to thank my advisor, Professor Papamoschou. He has been mentoring and guiding me ever since I was an undergraduate student who knew absolutely nothing. I would also like to thank all of my friends and family members who encouraged to take the leap and pursue a graduate education.

# CURRICULUM VITAE

**Tae Young Kim**

## EDUCATION

**Master of Science in Mechanical and Aerospace Engineering**  
University of California, Irvine

**2016**

*Irvine, California*

**Bachelor of Science in Mechanical and Aerospace Engineering**  
University of California, Irvine

**2014**

*Irvine, California*

## RESEARCH EXPERIENCE

**Graduate Student Researcher**  
University of California, Irvine

**2014–2016**

*Irvine, California*

## TEACHING EXPERIENCE

**Teaching Assistant**  
University of California, Irvine

**2015–2016**

*Irvine, California*

# NOMENCLATURE

## Abbreviations

BEMT	Blade Element Momentum Theory
BET	Blade Element Theory
BPF	Blade Passage Frequency
DAQ	Data Acquisition
ESC	Electronic Speed Control
FAA	Federal Aviation Administration
FAR	Federal Aviation Regulation
FFT	Fast Fourier Transform
OASPL	Overall Sound Pressure Level
OASPL(A)	A-Weighted Overall Sound Pressure Level
psi	Pounds Per Square Inch

## Symbols

<i>A</i>	Blade Section Area
<i>a</i>	$\frac{v_i}{V_\infty}$
<i>B</i>	Blade Count
<i>C</i>	Chord
<i>c</i>	Speed of Sound
<i>C<sub>d</sub></i>	Section Drag coefficient
<i>C<sub>l</sub></i>	Section lift coefficient
<i>C<sub>L<sub>α</sub></sub></i>	Lift-curve slope
<i>D</i>	Drag
<i>E</i>	Young's Modulus
<i>f</i>	Frequency
<i>F</i>	Prandtl's tip loss function
<i>I</i>	Area Moment of Inertia

$L$	Lift
$\dot{m}$	Mass flow rate through rotor
$p$	Static Pressure
$p'$	Acoustic Pressure Disturbance
$P_{Dm}$	Drag Noise Fourier Coefficient at harmonic $m$
$P_{Lm}$	Lift Noise Fourier Coefficient at harmonic $m$
$P_{Vm}$	Thickness Fourier Coefficient Noise at harmonic $m$
$q$	Transverse Beam Load
$T$	Propeller Thrust
$v_i$	Induced Velocity
$V_\infty$	Freestream Velocity
$w$	Slipstream velocity
$w$	Beam Deflection
$x, y, z$	Cartesian coordinate system position
$\alpha$	Angle of attack
$\alpha_i$	Induced Angle of attack
$\beta$	Blade pitch angle
$\delta$	$\Theta - \alpha_i$
$\varepsilon$	Separation Angle
$\eta$	efficiency
$\Theta$	Geometric Angle of Attack
$\theta$	Polar Angle
$\rho$	Density
$\sigma$	Stress
$\phi$	Azimuth angle
$\Omega$	Angular velocity

# **ABSTRACT OF THE DISSERTATION**

Reduction of Tonal Propeller Noise by Means of Uneven Blade Spacing

By

Tae Young Kim

Masters of Science in Mechanical and Aerospace Engineering

University of California, Irvine, 2016

Professor Dimitri Papamoschou, Chair

An experimental study was conducted on the noise characteristics of four-bladed general aviation propellers with uneven blade spacing. The subscale propeller designs were inspired by the four-bladed McCauley propellers used on the Beechcraft King Air 350 series aircraft. The 4-inch diameter (1:22.5 scale) propellers were manufactured using high-resolution stereolithography and were powered by a high performance, radio controlled brushless electric motor. Acoustic measurements were taken with a 24-microphone array. The use of uneven blade spacing created additional tones over which the acoustic intensity was distributed. Large amounts of acoustic intensity were shifted into the lowest frequency tone (occurring at half of the blade passage frequency of the propeller with evenly spaced blades), resulting in reductions of A-weighted overall sound pressure levels of up to 5 dB for polar angles near 90°. These reductions are partly offset by increases in A-weighted overall sound pressure levels of up to 4 dB at polar angles less than 50°. Although the theory used to predict propeller noise does not show good agreement with experiments, it does show this trend of increasing noise at low polar angles. Since noise at low polar angles are weighted less in noise metrics such as flyover noise, the use of uneven blade spacing has potential for providing noise reduction without adding excessive complexity to propeller design.

# **Chapter 1**

## **Introduction**

### **1.1 Motivation**

In the past few decades, the demand for air transportation in the United States has risen dramatically. This demand was met by an increase in the number of both commercial and general aviation aircraft, which in turn increased the noise pollution around airports and airport communities. Studies have shown that this increase in noise can devalue not only property [9, 25], but general health and quality of life as well [10, 13, 32]. To combat the increase in noise pollution, the Federal Aviation Agency introduced noise limit requirements for aircraft certification in the form of the Federal Aviation Regulations (FAR) Part 36 [12], and efforts in identifying and reducing aircraft noise sources have since been a topic of interest. The propeller is usually the most dominant source of noise in propeller driven aircraft and is therefore the subject of this study.

### **1.2 Background**

The propeller is the most efficient method of producing aerodynamic thrust at low subsonic speeds. A simple momentum analysis neglecting compressibility effects (shown in Appendix A), shows that the efficiency of any propulsion device is related to the ratio of the induced velocity at the propeller plane to the freestream velocity by equation 1.1. This ratio is called the induced velocity

factor and is denoted by the symbol  $a$  [30]. Equation 1.1 shows that higher theoretical efficiency is achieved by applying smaller acceleration to a larger mass of air. In the realm of low subsonic flight, where the effects of compressibility are not prominent, the propeller is the most practical method of imparting small acceleration to a large mass of air. Due to its high theoretical efficiency and relative simplicity, the propeller is still widely used in general aviation and military aircraft despite huge advances in jet engine technology.

$$\eta_{\text{propulsor}} = \frac{1}{1+a} \quad (1.1)$$

### 1.2.1 Elements of Propeller Noise

Propeller noise is often categorized into three components: harmonic or tonal noise, narrow-band noise, and broadband noise. The three components are described as follows by Magliozzi [18] and Smith [31].

Harmonic or tonal noise is caused by periodic motion of the propeller blades and is concentrated in deterministic frequencies. From a stationary point of view, a rotating propeller passes by with a frequency equal to the product of the shaft rotational frequency and the number of blades. This frequency is called the blade passage frequency or BPF. Each time a propeller blade passes, it generates pressure disturbances which propagate into the far-field as sound waves at the BPF and its harmonics. The main components of tonal noise are thickness, lift, and drag induced noise.

Narrow-band noise is caused by periodic motion of the propeller blades in unsteady flow conditions. Interaction between the flow and aircraft components such as the fuselage and misalignment of the propeller axis with respect to the incoming flow are examples that can cause unsteady blade loading. Because narrow-band noise is both deterministic and stochastic, it shows characteristics of both and occupies a narrow range of frequencies centered around the frequencies of tonal noise. In carefully controlled environments such as a research laboratory, narrow-band noise should be minimal.

Broadband noise is caused by the creation of, or interactions with turbulence. Since turbu-

lence is stochastic in nature, broadband noise is found at all frequencies. Atmospheric turbulence as well as turbulence created by aircraft components such as the fuselage and the propeller itself can contribute to broadband noise. Narrow-band and broadband noise will be neglected in this study because of the dominance of tonal noise propeller acoustics [23].

### 1.2.2 Previous Works

Conventional methods of reducing propeller and fan noise focused on isolating individual noise sources and reducing the source strengths. Attempts at lowering tonal noise include using thinner blade sections to lower thickness noise, and adjusting the number of blades, tip speed, blade chord, and other shape parameters to lower lift and drag induced noise [19]. Attempts at lowering broadband noise include suppressing the amount of turbulent vortex shedding by the blades [24]. However, these methods require significant design changes to the propellers, which tend to create losses in efficiency that outweigh the benefits in noise reduction. One method of noise reduction that is feasible is the use of blade sweep as shown by Wright and Simmons [34], and many modern propellers incorporate blade sweep. However, the main purpose of blade sweep is to improve propeller aerodynamics against the effects of compressibility, making noise reductions due to blade sweep an incidental benefit.

An alternative method of reducing propeller noise is to adjust the tonal characteristics of the propeller by unevenly spacing the blades around the hub. This preserves the geometry of the propeller blades and therefore does not harm propeller performance except in extreme configurations.

The concept of using unevenly spaced blades for noise reduction was first introduced by Mellin, et al [21], Ewald, et al [11] and Shahady, et al [29]. These studies showed that the use of uneven blade spacing distributed the tonal noise over a larger number of tones spread across a broader range of frequencies. This broadening of the tonal noise reduced perceived noise by giving it a higher degree of “whiteness.”

More recent work by Dobrzynski [8] and Cattanei, et al [7] have found promising results with uneven blade spacing, but commercial fixed-wing aircraft have not adopted the concept. Ap-

plications of uneven blade spacing can be found in helicopter tail rotors and in automotive cooling fans shown in figure 1.1 to ensure passenger comfort as described by Boltezar, et al [6] and Lee, et al [16]. The adoption of uneven blade spacing in helicopters and automobiles imply that they have potential in reducing tonal noise and should be investigated for use in commercial aviation.



Figure 1.1: Applications of uneven blade spacing found in the Nissan Sentra's radiator cooling fan (left) [22] and in the Eurocopter EC135 helicopter tail rotor (right), courtesy of Christoph Hansa. ([https://en.wikipedia.org/wiki/File:RTH\\_Christoph\\_Hansa\\_06.jpg](https://en.wikipedia.org/wiki/File:RTH_Christoph_Hansa_06.jpg).)

### 1.3 Objectives

This study aims to understand and reduce the perceived noise from general aviation propellers with uneven blade spacing. The following objectives are established:

- Demonstrate the viability of using rapid prototyping methods in subscale propeller experiments.
- Prove that the noise of propellers with uneven blade spacing can be predicted using simplified theoretical models.
- Investigate the effects of various uneven blade spacing angles on propeller noise intensity and directivity.

## 1.4 Thesis Overview

**Chapter 1:** Introduction of topic of interest.

**Chapter 2:** Summary of the theory used to predict propeller noise.

**Chapter 3:** Outline of the design procedures of subscale propellers.

**Chapter 4:** Details the experimental facilities and instruments.

**Chapter 5:** Analysis of experimental results.

**Chapter 6:** Summary of the findings in this study.

**Appendix A:** Blade element momentum theory and blade stress analysis.

**Appendix B:** Comparison of unweighted and weighted spectra.

**Appendix C:** Comparison with baseline propeller unweighted spectra.

**Appendix D:** Comparison with baseline compound propeller unweighted spectra.

# Chapter 2

## Theoretical Work

### 2.1 Noise Prediction of a Propeller with Even Blade Spacing

The harmonic noise of the propeller was predicted using far field helicoidal surface theory derived by Hanson [15]. The model theorizes that the pressure-time signal of the propeller is given by

$$p(t) = \sum_{m=-\infty}^{\infty} P_{mB} e^{-imB\Omega t} \quad (2.1)$$

where  $m$  is the harmonic or integer multiple of the blade passage frequency,  $B$  is the number of blades, and  $\Omega$  is the angular velocity. The Fourier coefficient  $P_{mB}$  can be expressed as the summation of the all noise sources:

$$P_{mB} = P_{Vm} + P_{Dm} + P_{Lm} + P_{11m} + P_{12m} + P_{22m} \quad (2.2)$$

$P_{Vm}$ ,  $P_{Lm}$ , and  $P_{Dm}$  are the Fourier coefficients of the sources due to thickness, lift, and drag respectively and represent the strength of each source for the  $m^{\text{th}}$  harmonic of the blade passage frequency. The coefficients are related to the source strengths  $\Psi_V$ ,  $\Psi_L$ , and  $\Psi_D$  by equations 2.3 to

2.5.

$$P_{Vm} = K_1 \int_{\bar{r}_{hub}}^{\bar{r}=1} K_2 k_x^2 t_b \Psi_V(k_x) d\bar{r} \quad (2.3)$$

$$P_{Lm} = K_1 \int_{\bar{r}_{hub}}^{\bar{r}=1} -\frac{i}{2} K_2 k_y C_L \Psi_L(k_x) d\bar{r} \quad (2.4)$$

$$P_{Dm} = K_1 \int_{\bar{r}_{hub}}^{\bar{r}=1} \frac{i}{2} K_2 k_x C_D \Psi_D(k_x) d\bar{r} \quad (2.5)$$

The integration is performed over the normalized radial coordinate  $\bar{r}$  and  $t_b$  is the ratio of maximum thickness to chord. The coefficients  $K_1$  and  $K_2$  are computed using equations 2.6 and 2.7, where  $L$  is the observer distance from the origin,  $y$  is the observer distance from the propeller axis,  $D$  is the propeller diameter,  $M_x$  is the flight Mach number, and  $\theta$  is the polar angle.

$$K_1 = -\frac{\rho c^2 B \sin \theta \exp[imB(\frac{\Omega L}{c}) - \frac{\pi}{2}]}{8\pi \frac{y}{D} (1 - M_x \cos \theta)} \quad (2.6)$$

$$K_2 = M_{\bar{r}}^2 J_{mb} \left( \frac{m B \bar{r} M_T \sin \theta}{1 - M_x \cos \theta} \right) \quad (2.7)$$

The wavenumbers  $k_x$  and  $k_y$  are computed using equations 2.8 and 2.9, where  $B_D$  is the chord to diameter ratio and  $M_{\bar{r}}$  is the blade section Mach number.

$$k_x = \frac{2m B B_D M_T}{M_{\bar{r}} (1 - M_x \cos \theta)} \quad (2.8)$$

$$k_y = \frac{2m B B_D}{\bar{r} M_{\bar{r}}} \left( \frac{M_{\bar{r}}^2 \cos \theta - M_x}{M_{\bar{r}} (1 - M_x \cos \theta)} \right) \quad (2.9)$$

The source strength for thickness noise is determined using a distribution of monopole sources. The physical blade surfaces are replaced by a distribution of monopole sources that have the same effect on the fluid. Using the thin blade assumption, the sources can be distributed along the propeller blade section chord as shown in figure 2.1 rather than the upper and lower surfaces. The effect of the source distribution is integrated over the section chord to represent the blade section

geometry.

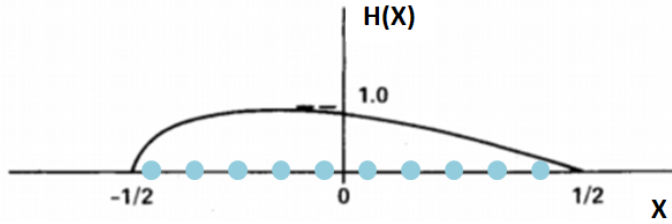


Figure 2.1: Distribution of monopole sources (blue dots) along the normalized chord  $X$ .  $H(X)$  represents the normalized thickness distribution.

The strength of the monopole source  $\Psi_V$  as a function of the wavenumber  $k_x$  is given by equation 2.10.

$$\Psi_V(k_x) = \int_{-1/2}^{1/2} H(X) e^{ik_x X} dX \quad (2.10)$$

The source strengths for the loading noise are determined using distributions of dipole sources. The effects of the source distributions are integrated over the section chord to represent the distribution of net pressure from the upper and lower surfaces of the blade section as shown in figure 2.2. This distribution of net pressure can be predicted using a combination of blade element momentum theory and the assumption that the pressure distribution along the chord is parabolic. In addition, the noise due to drag is considered negligible on the assumption that the drag is small compared to the lift. These assumptions were also made by Hanson and resulted in good correlation between experiment and theory [15].

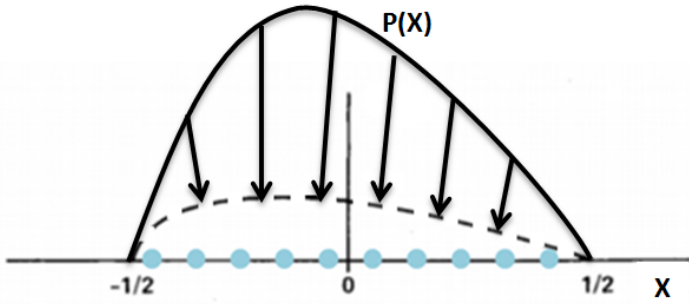


Figure 2.2: Distribution of dipole sources (blue dots) along the normalized chord  $X$ .  $P(X)$  represents the normalized net pressure distribution acting on the blade section.

$$\Psi_L(k_x) = \int_{-1/2}^{1/2} P(X) e^{ik_x X} dX \quad (2.11)$$

The strength of the dipole source for lift  $\Psi_L$  as a function of the wavenumber  $k_x$  is given by equation 2.11.

The source strengths for the noise due to shear stresses in the propeller wake are determined using distributions of quadrupole sources. However, the calculation of quadrupole source strengths require the knowledge of the Lighthill's stress tensor which is beyond the scope of this study. Therefore the quadrupole terms  $P_{11m}$ ,  $P_{12m}$ , and  $P_{22m}$  will be ignored.

## 2.2 Superposition of Propellers with Even Blade Spacing

It is important to note that equation 2.1 only applies to propellers with even blade spacing. However, a simple method described by Dobrzynski allows for the superposition of propellers with even blade spacing to create propellers with uneven blade spacing [8]. If the noise of an evenly spaced, two-bladed propeller is known (can be predicted by Hanson's theory), the pressure signal from this propeller can be added to itself with a phase shift corresponding to the desired separation angle in the propeller with uneven blade spacing. The combined pressure signal resembles a signal

from an unevenly spaced, four-blade propeller and is shown in equation 2.12.

$$p(t) = \sum_{m=-\infty}^{\infty} P_{m(2)} e^{-im2\Omega t} + \sum_{m=-\infty}^{\infty} P_{m(2)} e^{-im2(\Omega t+\varepsilon)} \quad (2.12)$$

To verify that equation 2.12 produces dependable results, the solution to equation 2.12 with  $B = 2$  and  $\varepsilon = 90^\circ$  is compared to the solution to Hanson's original theory (equation 2.1) with  $B = 4$ . All variables except the number of blades and separation angle were identical between the two cases. The peaks corresponding to tonal noise in figure 2.3 are identical and therefore validate equation 2.12. The regions between the peaks are a result of errors in the Fourier Transform of a finite pressure signal and do not represent broadband noise.

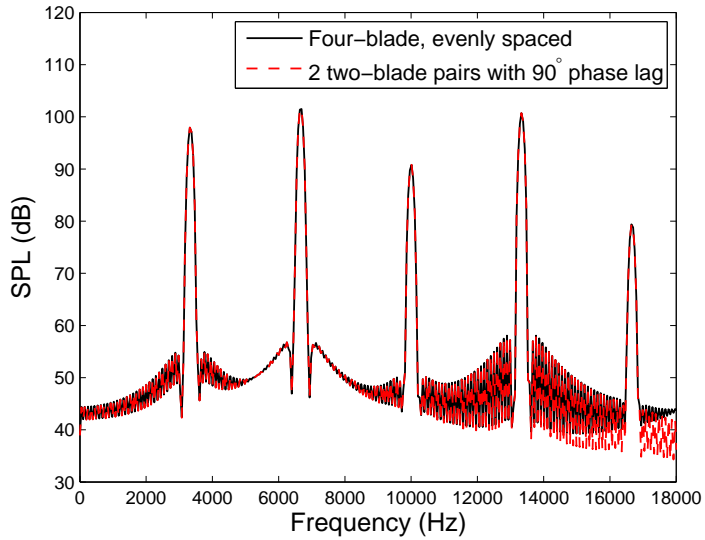


Figure 2.3: Acoustic phase shift validation

## 2.3 Results of Theoretical Analysis

The method of superimposing propeller noise signals was employed to predict the A-weighted overall sound pressure levels OASPL(A) for separation angles  $10^\circ < \varepsilon < 90^\circ$  and polar angles  $20^\circ < \theta < 160^\circ$ . To determine the effectiveness of the uneven blade spacing, the OASPL(A) of the propellers with uneven blade spacing were compared to those of the propeller with even blade

spacing by equation 2.13.

$$\Delta \text{OASPL}(A) = \text{OASPL}(A) - \text{OASPL}(A)_{\epsilon=90^\circ} \quad (2.13)$$

This quantity,  $\Delta \text{OASPL}$ , represents the change in noise quantity of each propeller from the baseline propeller with evenly spaced blades at various polar angles and is shown in figures 2.4 and 2.5.

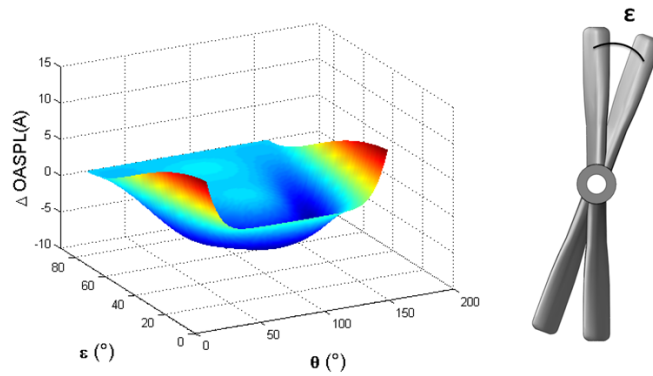


Figure 2.4:  $\Delta \text{OASPL}(A)$  map. Negative values of  $\Delta \text{OASPL}(A)$  denote reductions in noise while positive values denote increases in noise.

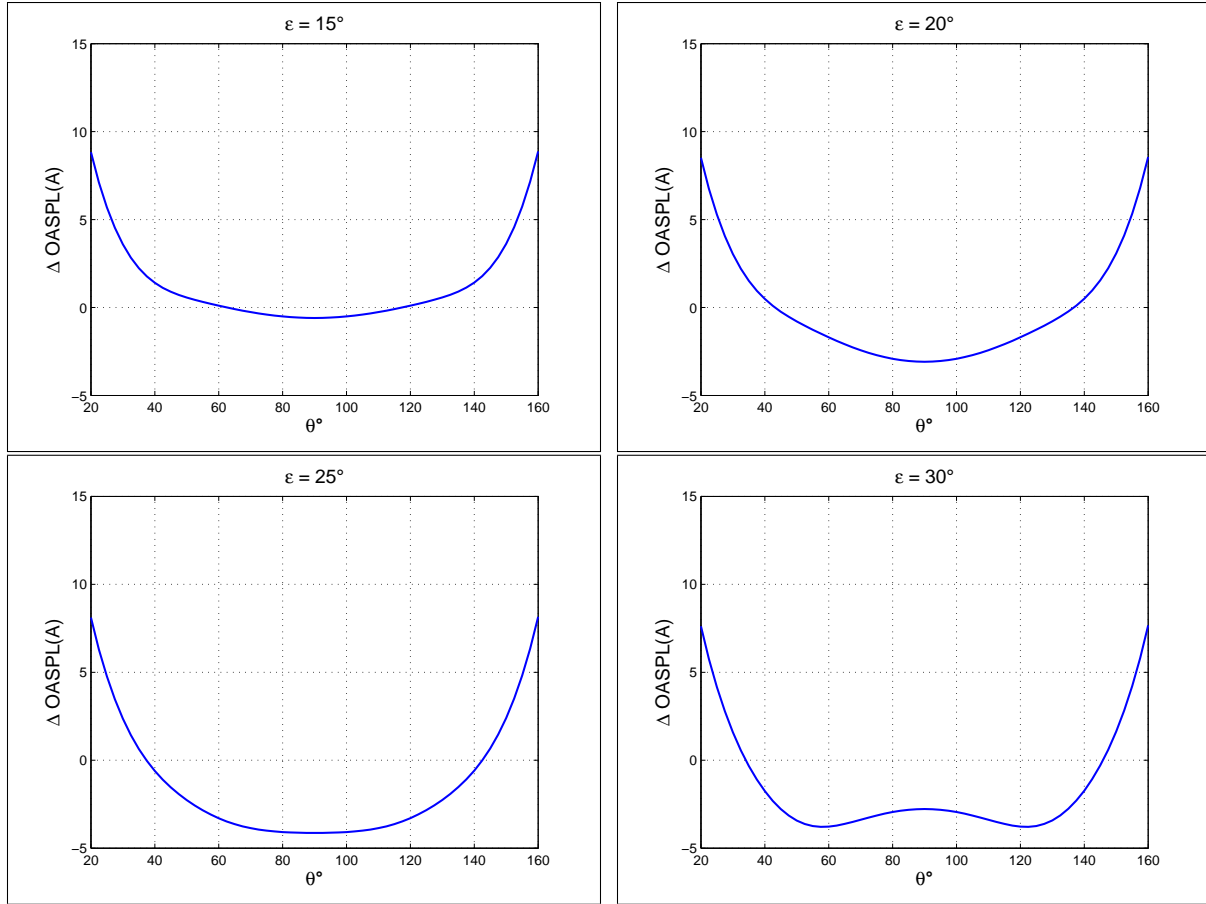


Figure 2.5:  $\Delta \text{OASPL}(A)$  for  $\varepsilon = 15^\circ, 20^\circ, 25^\circ, 30^\circ$ .

The location of maximum OASPL(A) reductions vary with separation angle, but the reductions tend to be concentrated near the plane of the propeller ( $\theta = 90^\circ$ ). At very low and very high polar angles, increases in OASPL(A) are found for all separation angles.

# **Chapter 3**

## **Propeller Design**

### **3.1 McCauley Propeller**

The subscale propellers were designed based on a 4-blade McCauley Propeller (model SA1241GL) used on the twin-engine Beechcraft King Air 350 series aircraft. The latest models feature propellers with swept blades from the Raisbeck Engineering Company. However, the propeller by McCauley Propeller Systems used on older models, shown in figure 3.1, was chosen over the Raisbeck propeller for its geometric simplicity [20].



Figure 3.1: The latest update to the 350 series, the Beechcraft King Air 350i [4].

The Pratt and Whitney PT6A engines that power the propellers each provide 550 shaft horsepower at an RPM of 2200. This propeller and engine combination produces a disc loading of 0.23 psi and a tip Mach number of 0.77. The subscale propellers were designed to meet these two criteria for acoustic similarity.

## 3.2 Subscale Propellers

The subscale baseline propeller has a diameter of 4 inches and is geometrically similar to the McCauley propeller. It was designed using the NACA 64A410 airfoil to create the required tip speed and disc loading at 50,000 RPM. To prevent the propeller blades from bending from axial (thrust) loads and failing under centrifugal loads, the chord and thickness distributions were modified as shown in figure 3.2. Final stress predictions were made using the finite element analysis tool in Solidworks, which predicted a factor of safety of approximately 1.2 under centrifugal loads at 50,000 RPM.

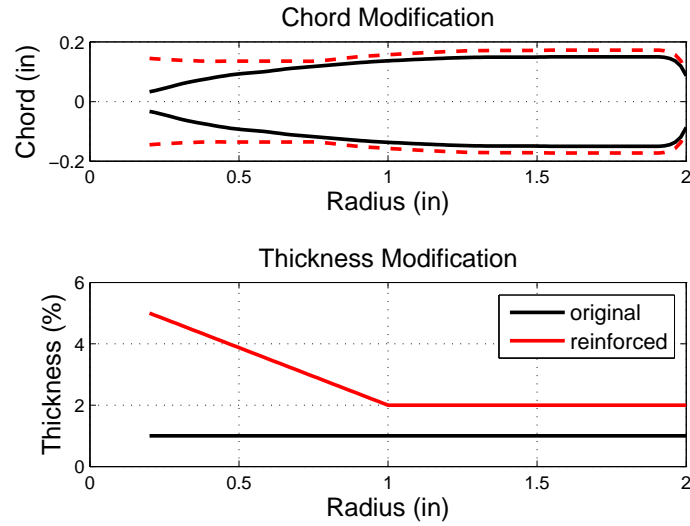


Figure 3.2: Chord and thickness modifications.

The propeller twist distribution of the McCauley propeller is unknown, so the twist of the subscale propeller was determined using blade element-momentum theory (described in Appendix A). The twist distribution that produces the required disc loading at the optimum aerodynamic efficiency was found to be a logarithmic curve shown in black in figure 3.3. This distribution was then modified to favor higher amounts of twist towards the hub to create a more stiff structure that is less likely to bend under axial (thrust) loads. The twist towards the tip was reduced to maintain the desired disc loading. The modified twist distribution is shown by the red logarithmic curve in figure 3.3.

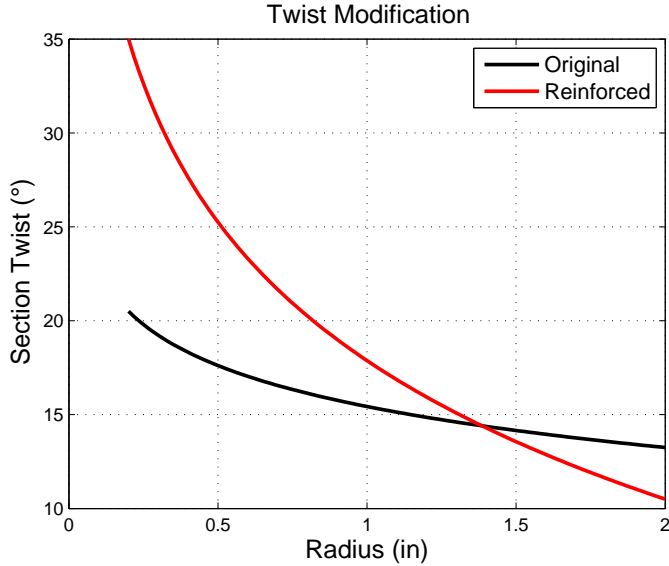


Figure 3.3: Twist modification.

Three propeller designs were chosen to be manufactured using stereolithography. The first design was the baseline propeller with evenly spaced blades that served as a reference for all other propellers. The remaining two propellers were propellers with uneven blade spacing. With the guidance of the results in Chapter 2, the propellers with uneven blade spacing were chosen to have separation angles of  $20^\circ$  and  $30^\circ$ . All other parameters were kept constant for all propellers. Separation angles less than  $20^\circ$  were not taken into consideration for experimental testing due to speculations that such small angles would cause too much aerodynamic interference between the blades and result in significant losses in efficiency. The propellers were manufactured using the high resolution stereolithography services from Proto Labs, Inc. The details of the stereolithography material (called Accura 60) are specified in Reference [1].

Due to the finite resolution of the manufacturing process, tolerances are limited to a minimum thickness of 0.016 inches. To account for this limitation, the propeller leading and trailing edges, where the blade section airfoil profile converges to a single point, were thickened to 0.016 inches. An example of this is shown in figure 3.4.

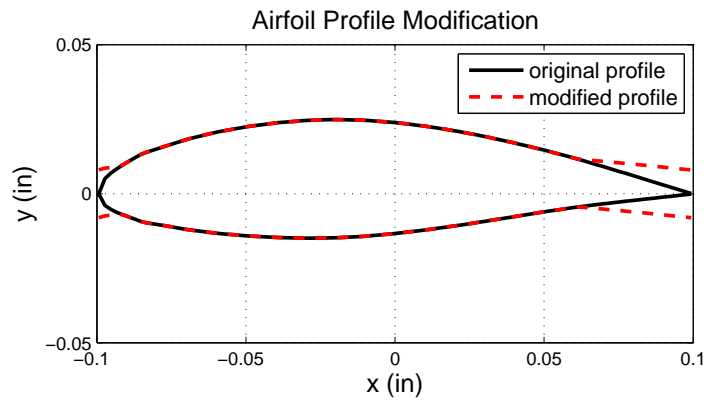


Figure 3.4: Airfoil profile modification.

The propellers were sanded to restore its original geometry at the leading and trailing edges and to minimize drag due to surface roughness. Final 3D drawings and pictures of printed propellers are shown in figures 3.5 and 3.5 respectively.

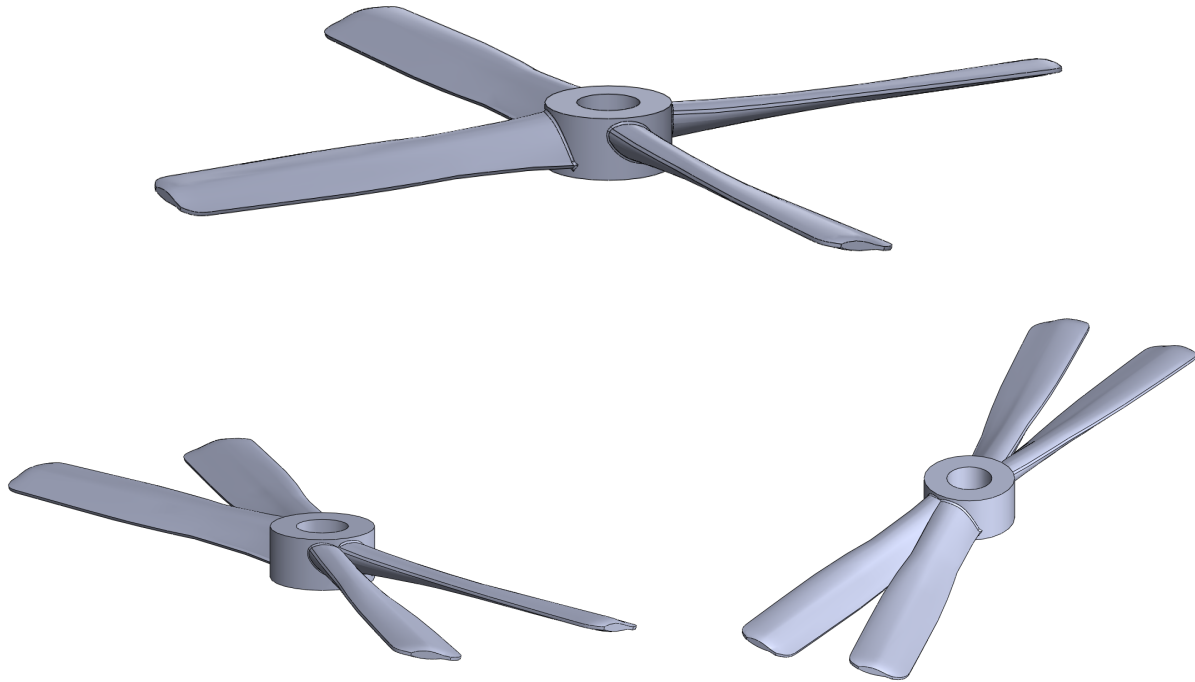


Figure 3.5: 3D drawings of propellers with separation angles:  $90^\circ$  (top),  $30^\circ$  (bottom left),  $20^\circ$  (bottom right). Drawings were generated on Solidworks.

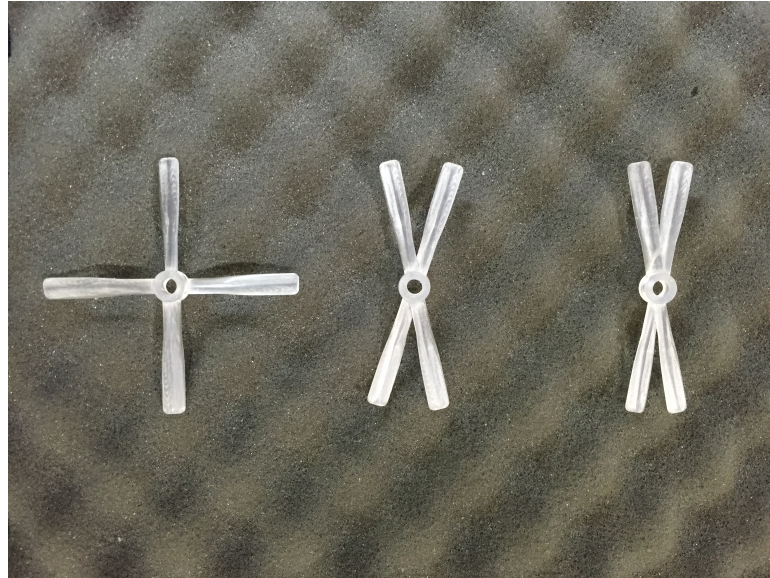


Figure 3.6: Printed propellers with separation angles:  $90^\circ$  (left),  $30^\circ$  (center),  $20^\circ$  (right).

After testing was completed, it was discovered that the blade element momentum theory used in the design process was creating an over prediction of thrust. This was corrected by applying the Betz condition for minimum energy loss [27]. However, it must be noted that the propellers that were tested experimentally were designed to meet an incorrect value of disc loading due to the over prediction of thrust.

# Chapter 4

## Experimental Details

### 4.1 Power Plant

The propellers were powered by a Hoffman Magnetics EDF 70HW "Wild Beast" DC brushless motor, Castle Creations Pheonix 125 electronic speed controller (ESC), and a 4-cell lithium polymer battery. The "Wild Beast" is capable of handling up to 1700 Watts and 60,000 RPM. Motor throttle controls were transmitted and received using the Spektrum DX7 2.4 GHz 7 channel radio transmitter and Spektrum AR6200 DSM26 receiver. The schematic of this system is shown in figure 4.1.

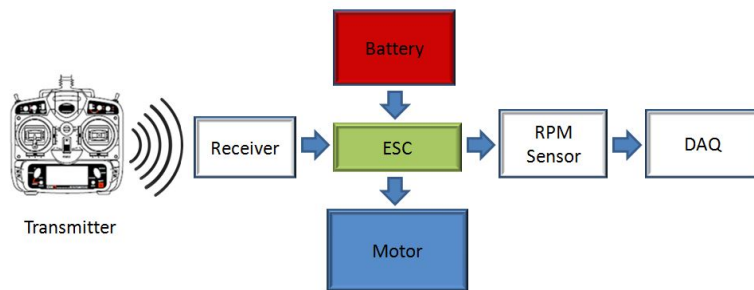


Figure 4.1: Electronics block diagram.

## 4.2 Data Measurement and Collection

### 4.2.1 Acoustic Pressure Measurement

Acoustic pressure was measured using the Brüel & Kjaer type 4138 microphone with a frequency response of 140 kHz and Brüel & Kjaer type 2690-A-0S4 amplifier. 24 microphones and 6 amplifiers were housed in an anechoic chamber lined with Illbruch SONEX super, 6-inch tall polyurethane foam acoustic wedges. The chamber inlet and outlet, where the usage of tall wedges are impractical, were lined with ILLbruck SONEX mini acoustic baffles. Microphone locations are defined by the polar angle  $\theta$  and the azimuth angle  $\phi$  as shown in the schematic in figure 4.2. Twelve microphones were arranged on the downward arm ( $\phi = 0^\circ$ ) and twelve on a sideline arm ( $\phi = 60^\circ$ ) at polar angles of approximately  $20^\circ < \theta < 120^\circ$ .

To minimize the noise from the interactions between the flow and the supporting structure, the motor was supported by an aerodynamic strut hanging down from the ceiling. All of the sensors and electronics were located on the ceiling or high on the strut and the wires connecting to the motor were run internally in the strut to create the cleanest environment possible.

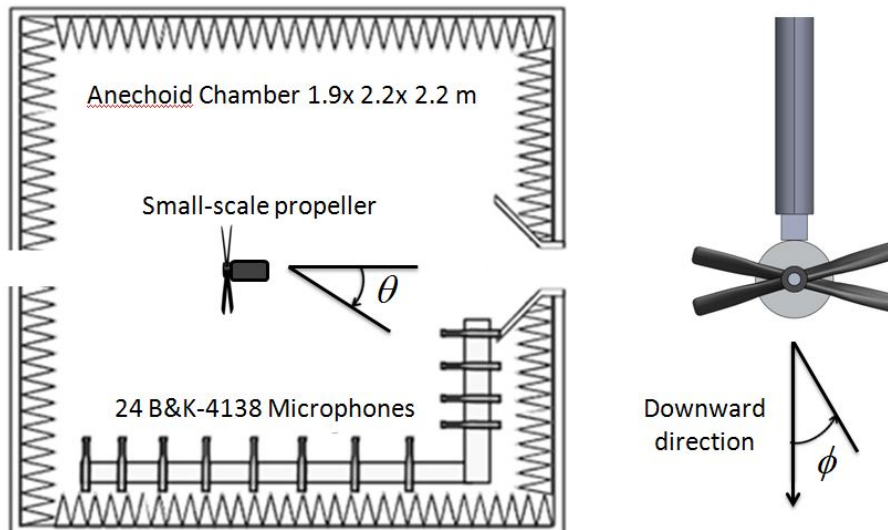


Figure 4.2: Anechoic chamber schematic.

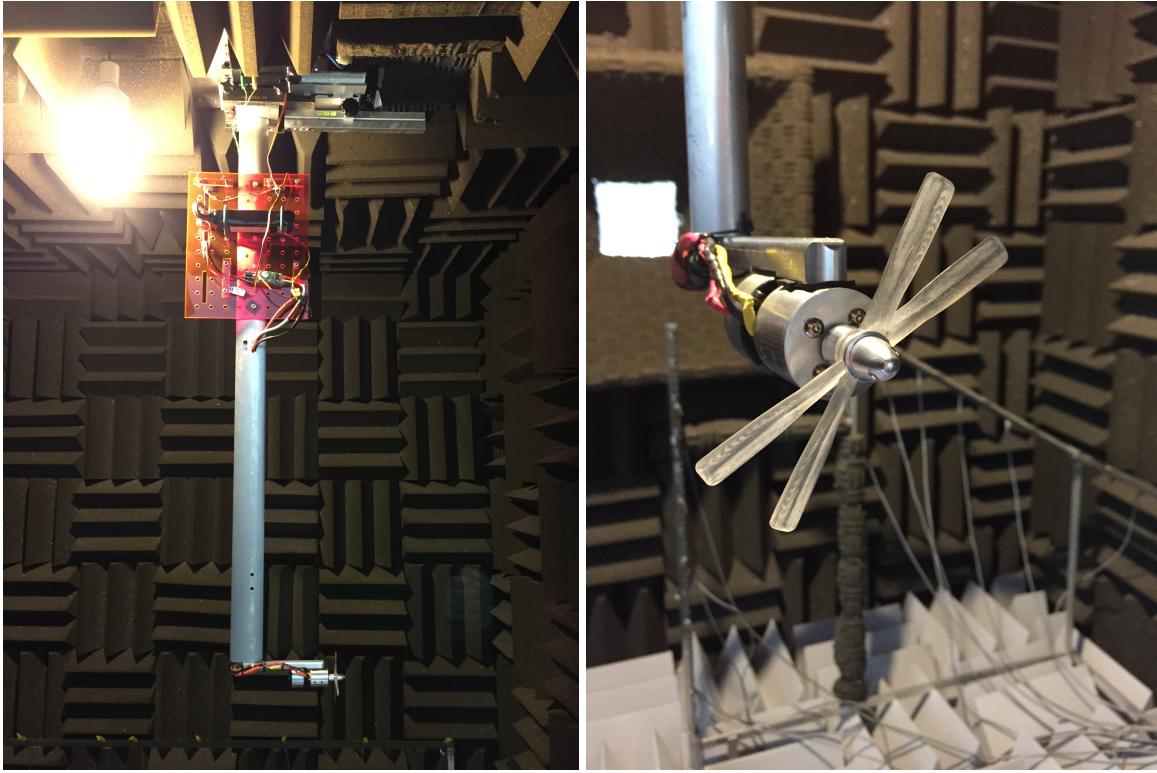


Figure 4.3: Anechoic chamber setup with the  $\epsilon$ 30 propeller.

#### 4.2.2 Thrust Measurement

Propeller thrust was measured by a Transducer Techniques ESP-35 beam load cell with a maximum load of 77 pounds and OMEGA Engineering DP25B-S strain gauge panel meter. The load cell was located at the top above the strut and is oriented as shown in figure 4.4. The propeller thrust is amplified by the strut, hinge, and arm assembly and is transmitted to the load cell. The system was designed to allow the load cell to move closer or farther from the hinge axis, and doing so changes the amplification factor of the force due to the change in moment arm. To minimize instrument error from the load cell, this amplification factor was carefully chosen to amplify the expected propeller thrust close to the load cell's maximum load of 77 pounds.

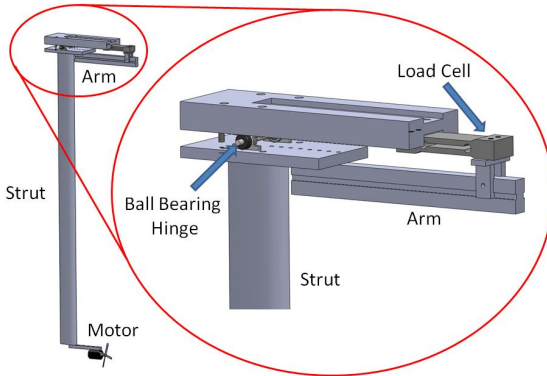


Figure 4.4: Motor support and thrust measurement assembly.

### 4.2.3 RPM Measurement

The propeller RPM was calculated using the rate of fluctuation of the power signal being fed into the motor. A coil of magnet wire wrapped around one of the motor leads was used to sense the fluctuating voltage by magnetic induction. This signal was then conditioned using a voltage divider, buffer, and low-pass filter and was processed using a fast Fourier Transform code to obtain the frequency of the fluctuation as depicted in figure 4.5. Due to the nature and design of brushless motors, the motor RPM is related to the fluctuation frequency by equation 4.1. The "Wild Beast" motor has four magnetic poles, so the RPM can be found by equation 4.2.

$$\text{RPM} = \text{Frequency} * \left( \frac{2 * 60}{\text{number of poles}} \right) \quad (4.1)$$

$$\text{RPM} = \text{Frequency} * 30 \quad (4.2)$$

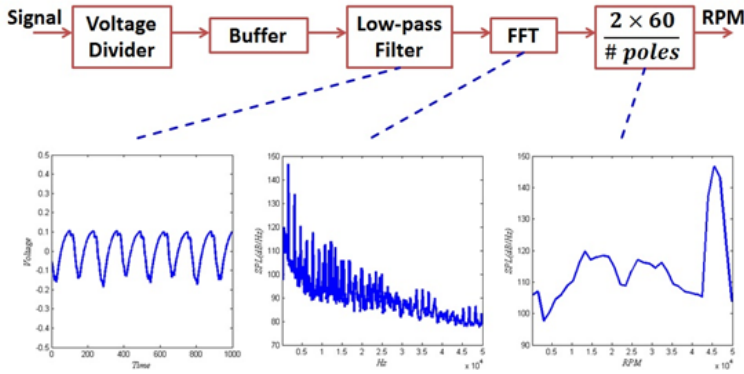


Figure 4.5: RPM sensor block diagram, designed by Truong [33].

## 4.3 Data Processing

Raw data from the microphones must be processed in order to provide meaningful results. This section will describe three important acoustic metrics used to evaluate the effectiveness of uneven blade spacing in reducing propeller noise. These metrics are the sound pressure level (SPL), overall sound pressure level (OASPL), and acoustic pressure.

### 4.3.1 Sound Pressure Level

The sound pressure level distribution, or power spectrum, represents the distribution of acoustic energy over frequency. It is obtained using a 4096-point fast Fourier transform of the acoustic pressure fluctuation as shown in equation 4.3, where the reference pressure  $p_{\text{ref}}$  is  $20 \mu\text{Pa}$ .

$$\text{SPL}_{\text{raw}}(f) = \lim_{T \rightarrow \infty} \frac{1}{T} \left| \int_{-T}^{T} \frac{p(t)}{p_{\text{ref}}} e^{-i2\pi f t} dt \right|^2 \quad (4.3)$$

The spectrum must be corrected for microphone frequency response, microphone freefield response, and atmospheric absorption. The frequency and freefield response corrections were performed based on microphone specifications provided by the manufacturer, and the atmospheric absorption correction was performed using the relation in Bass et al. [5] based on the relative hu-

midity and temperature readings measured at the time of testing. The corrected spectrum, shown by equation 4.4, represents the small scale lossless power spectrum. To obtain the full scale spectrum, equation 4.4 is divided by the scale factor [26].

$$\text{SPL}(f) = \text{SPL}_{\text{raw}}(f) + C_{\text{FR}}(f) + C_{\text{FF}}(f) + C_{\text{AA}}(f) \quad (4.4)$$

$C_{\text{FR}}$  = Correction for microphone frequency response

$C_{\text{FF}}$  = Correction for microphone freefield response

$C_{\text{AA}}$  = Correction for atmospheric absorption

The acoustic intensity within a given frequency band  $[f_1, f_2]$  is calculated by integrating the SPL spectrum over this band. This result can be presented as the square of the raw pressure fluctuation within this band

$$p_{\text{rms}}^2 = p_{\text{ref}}^2 \int_{f_1}^{f_2} 10^{\text{SPL}(f)/10} df \quad (4.5)$$

This procedure is used to calculate the energy content of tonal noise in section 5.2.

### 4.3.2 Overall Sound Pressure Level

The overall sound pressure level provides a measure of the variance of the pressure signal. It is calculated by integrating the power spectrum as shown in equation 4.6. The limit  $f_{\text{upper}}$  refers to the highest frequency resolved in the experiments.

$$\text{OASPL} = 10 \log_{10} \left( \int_0^{f_{\text{upper}}} 10^{\text{SPL}/10} df \right) \quad (4.6)$$

However, this measure of noise does not take the human ear's frequency response into account. Human ears are more sensitive to certain frequencies, and one way to account for this is to "correct" the power spectrum using A-weighting. This method adds or subtracts decibels from the power spectrum at each frequency based on the weight curve shown in figure 4.6.

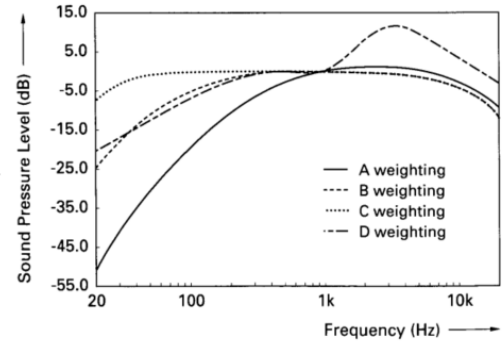


Figure 4.6: A-weighting correction curve [2].

The A-weighted power spectrum  $\text{SPL(A)}$  can be used to calculate the A-weighted overall sound pressure level  $\text{OASPL(A)}$ .

$$\text{OASPL(A)} = 10 \log_{10} \left( \int_0^{f_{\text{upper}}} 10^{\text{SPL(A)/10}} df \right) \quad (4.7)$$

# Chapter 5

## Results and Analysis

For simplicity, the subscale propellers with  $20^\circ$  and  $30^\circ$  of uneven blade spacing will be referred to as the  $\epsilon 20$  and  $\epsilon 30$  propellers respectively. The baseline propeller with evenly spaced blades will be referred to as the  $\epsilon 90$  propeller. This chapter will focus on the analysis of acoustic intensity and OASPL. The power spectra will be reserved for Appendices B, C, and D.

### 5.1 Tip Mach Number and Disc Loading

Experimental thrust and disc loading results are plotted in figure 5.1 along with predicted values from blade element momentum theory. The theory predicts the same thrust for all separation angles because it neglects interactions between blades. Although experiments show good agreement with theory, the target disc loading value of 0.23 psi was not reached experimentally. During a test, the motor shaft sheared off and destroyed the  $\epsilon 30$  propeller in the process. The thrust and disc loading data were only taken up to 36,600 RPM, while the acoustic data (collected separately from thrust data) were taken up to a slightly higher RPM of around 39,000.

The tip Mach number and disc loading of the subscale propellers are listed in table 5.1. Tests showed that the propellers with uneven blade spacing typically produce lower thrust at a given RPM, with the  $\epsilon 20$  propeller experiencing a rather large thrust loss of 8.5% compared to the  $\epsilon 90$  propeller at 36,600 RPM. At first, the loss of thrust was believed to be the result of some turbulence

related effects, such as the ingestion of the leading blade's trailing edge separation by the trailing blade. But the lack of narrowband noise in the  $\varepsilon 20$  and  $\varepsilon 30$  spectra (found in appendix B) suggests otherwise.

Propeller	RPM	Tip Mach Number	Disc Loading at 36,600 RPM
$\varepsilon 90$	38,800	0.60	0.103 psi
$\varepsilon 30$	38,500	0.60	0.096 psi
$\varepsilon 20$	39,800	0.61	0.094 psi
Target	50,000	0.77	0.23 psi at 50,000 RPM

Table 5.1: RPM, tip Mach number, and disc loading.

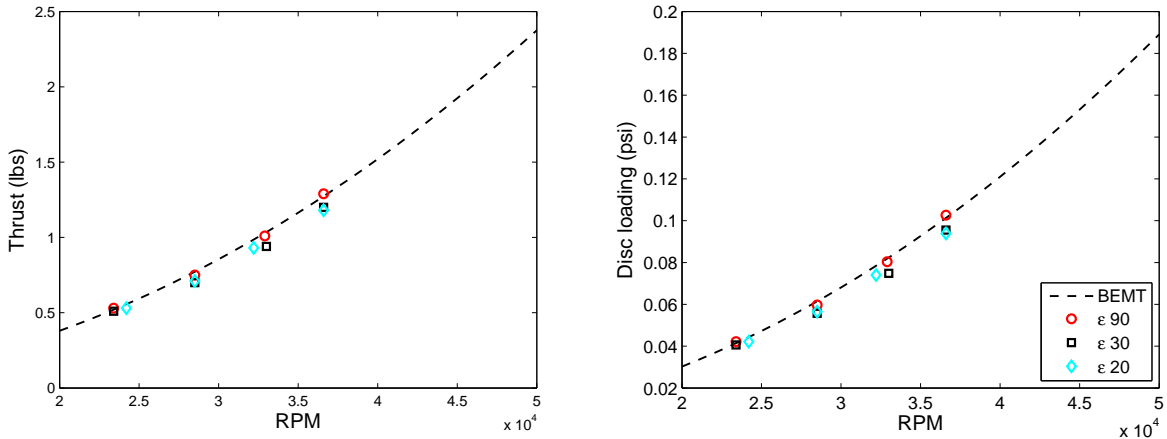


Figure 5.1: Comparison of thrust (left) and disc loading (right) between theory and experiments.

Instead, the thrust loss is believed to be caused by the leading blade's downwash. The blade element momentum theory that was used to determine the geometric twist distribution along the propeller blades assumed that individual blades do not interact with each other in any way. So the propeller blades sections have angles of attack that are designed to operate in undisturbed flow from a rotating frame of reference. However, the adjacent blades of the  $\varepsilon 30$  and  $\varepsilon 20$  propellers

are so close to each other near the hub that the trailing blade gets caught in the downwash of the leading blade. The trailing blade therefore operates with smaller angles of attack and produces less than the expected amount of lift. This loss of lift in the trailing blade is believed to result in the overall propeller thrust loss of up to 8.5% at 36,000 RPM and possibly more at higher speeds. Future designs should have modified twist distributions on the trailing blades to account for the downwash effects from the leading blades.

## 5.2 Power Spectra

The  $\varepsilon$ 30 and  $\varepsilon$ 20 propellers produce twice as many tones as the  $\varepsilon$ 90 propeller, at locations in-between the tones found in the  $\varepsilon$ 90 propeller. To make it easier to refer to individual tones, the blade passage frequency (BPF) and its harmonics of the  $\varepsilon$ 90 propeller will be referred to by 1BPF, 2BPF, 3BPF, and on. Since the  $\varepsilon$ 30 and  $\varepsilon$ 20 propellers produce tones that fall in between these tones, the tones of the  $\varepsilon$ 30 and  $\varepsilon$ 20 propellers will be referred to by 0.5BPF, 1BPF, 1.5BPF, and on. These tones are labeled in an example shown in figure 5.2.

The tones that are not labeled in figure 5.2 are unexpected tones and do not correlate to any type of tonal noise that the propellers should be emitting. These tones are believed to be a result of imbalance in the propeller blades causing vibrations in the propellers and the rig.

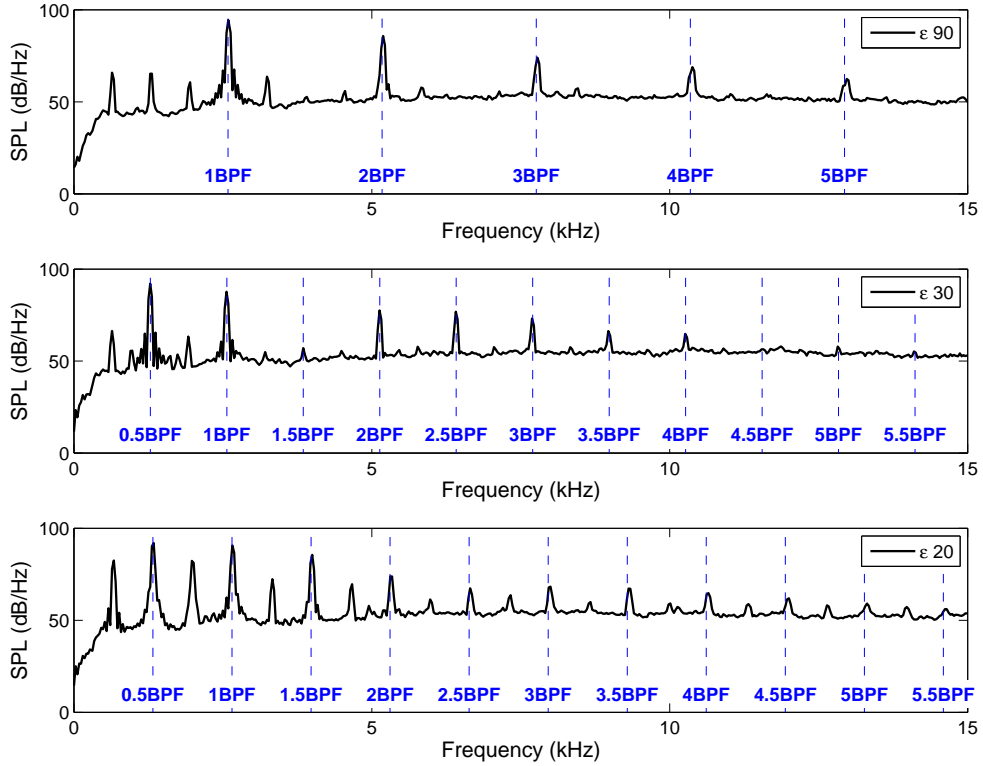


Figure 5.2: Spectra for  $\epsilon 90$  (top),  $\epsilon 30$  (middle), and  $\epsilon 20$  (bottom) with labeled tones for downward noise at  $\theta = 96.7^\circ$ .

An initial inspection of the spectra showed significant increases in broadband noise in the  $\epsilon 30$  and  $\epsilon 20$  propellers. Example spectra showing increases in broadband noise are shown in figure 5.3 (the rest can be found in Appendix C). Since the increase in broadband noise appears to be higher on average in the  $\epsilon 20$  propeller than the  $\epsilon 30$  propeller, it was hypothesized that this increase in broadband noise is due to some unknown interaction effect regarding the close proximity of the propeller blades. The adjacent blades in propellers with unevenly spaced blades come very close to each other near the hub and ultimately merge together as shown in figure 5.4. This close proximity at the propeller hub is hypothesized to result in increases in broadband noise.

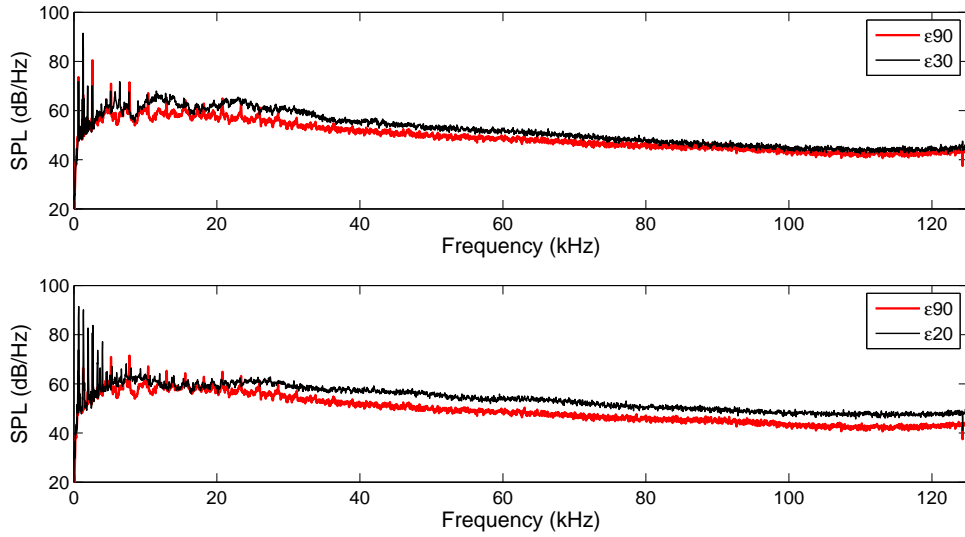


Figure 5.3: Spectra showing the increases in broadband noise in  $\varepsilon_{30}$  (top) and  $\varepsilon_{20}$  (bottom) for downward noise at  $\theta = 44.2^\circ$ .

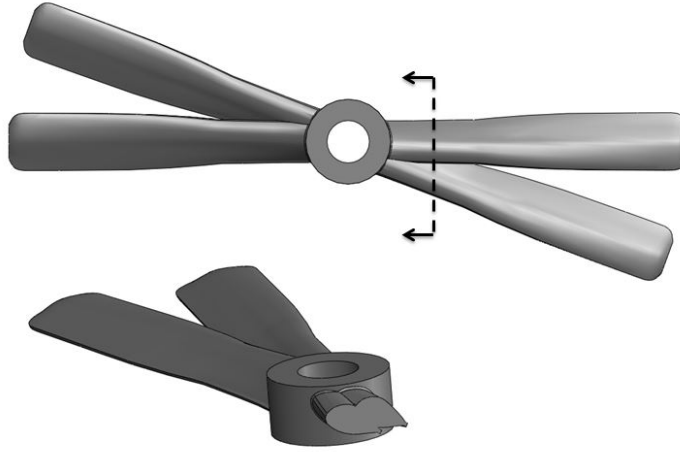


Figure 5.4: Section view of propeller showing the merging of blades near the hub.

In efforts to prove this hypothesis, additional experiments were conducted using hobby-grade RC propellers, as shown in figure 5.5. Two sets of two-bladed propellers (4.2x4 propellers by APC Propellers) were mounted onto a single motor shaft in tandem. Because the two sets of propeller blades are on separate hubs, the adjacent blades are naturally given some axial separation between them. These propellers will be referred to as the compound propeller, since each four-bladed propeller is formed by two separate two-bladed propellers. For example, the compound propeller

with  $30^\circ$  of separation will be labeled as “compound  $\varepsilon 30$ ” in figures.

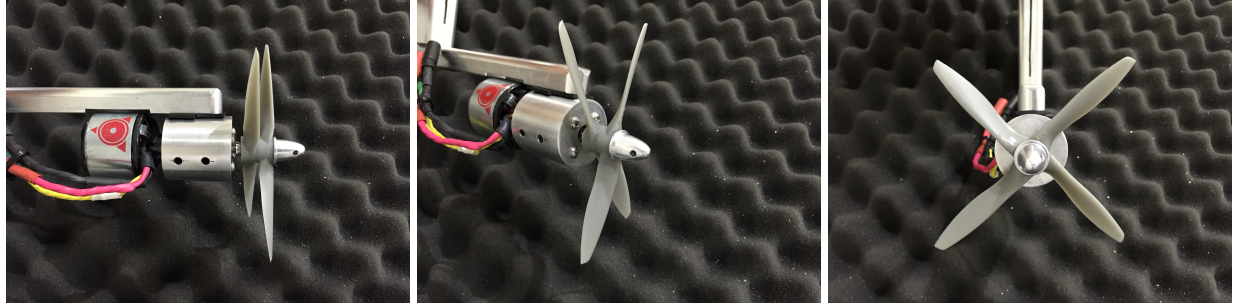


Figure 5.5: Compound propeller mounted onto motor for testing.

The separation between the adjacent blades in the compound propellers were adjusted to match those of the 3D printed propellers ( $20^\circ$  and  $30^\circ$ ). Due to the relatively high drag on the RC propellers however, the motor was only able to spin the compound propellers up to 29,300 RPM. Example spectra are shown in figure 5.6 (the rest of the spectra can be found in appendix D). At 29,300 RPM, the compound propellers show no signs of increases in broadband noise.

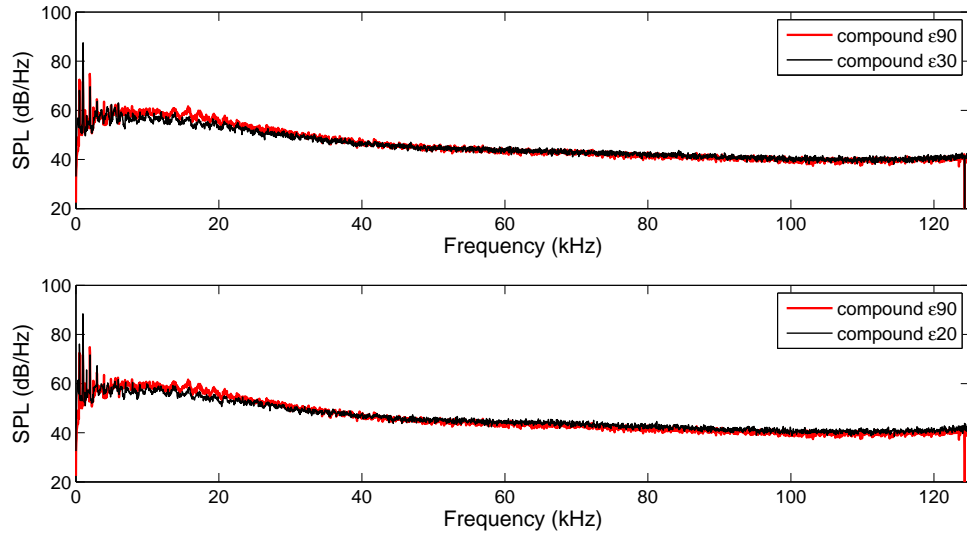


Figure 5.6: Compound propellers:  $\varepsilon 30$  (top) and  $\varepsilon 20$  (bottom) for downward noise at  $\theta = 44.2^\circ$ .

Future designs should incorporate some degree of axial spacing to prevent as much increases in broadband noise as possible. To keep the following analysis of data relevant, only the tonal noise will be considered. Tones were extracted by taking data within a fixed width of 120 hz centered

around peak frequencies as shown in figure 5.7. The width of 120 hz was chosen because the half-width of 60 hz consistently gave values of SPL that were more than 10 dB less than that of the peak. Extracted tones in figure 5.8 are shown shaded in red as an example. Tones that are thought to be the result of propeller imbalance and rig vibrations (and therefore not predicted by theory) were not extracted.

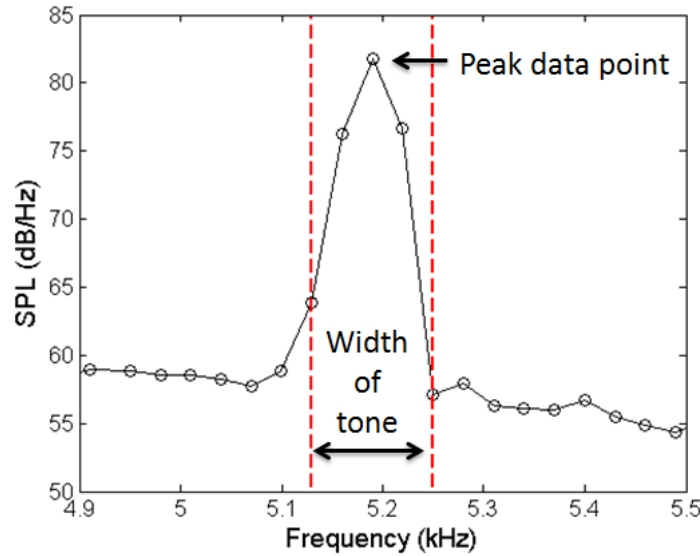


Figure 5.7: Extraction of tonal noise from power spectrum. The fixed width of 120 hz translates into 4 data points for a 4096 point-Fourier transform.

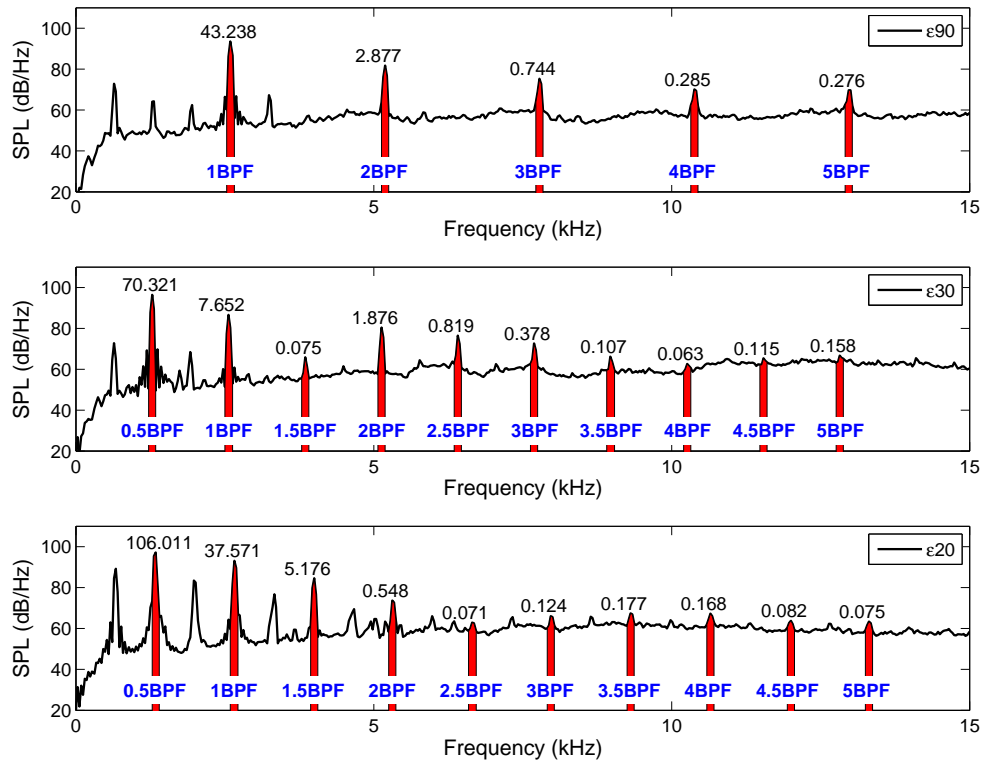


Figure 5.8: Filtered spectra for downward noise at  $\theta = 96.7^\circ$ . Extracted tones are shaded in red. The acoustic intensity for each tone is displayed above the tone in  $\text{Pa}^2$ .

The acoustic intensity in each tone was summed and plotted in figure 5.9 for all directions. The decrease in separation angle shifts the direction of maximum total acoustic intensity to lower polar angles.

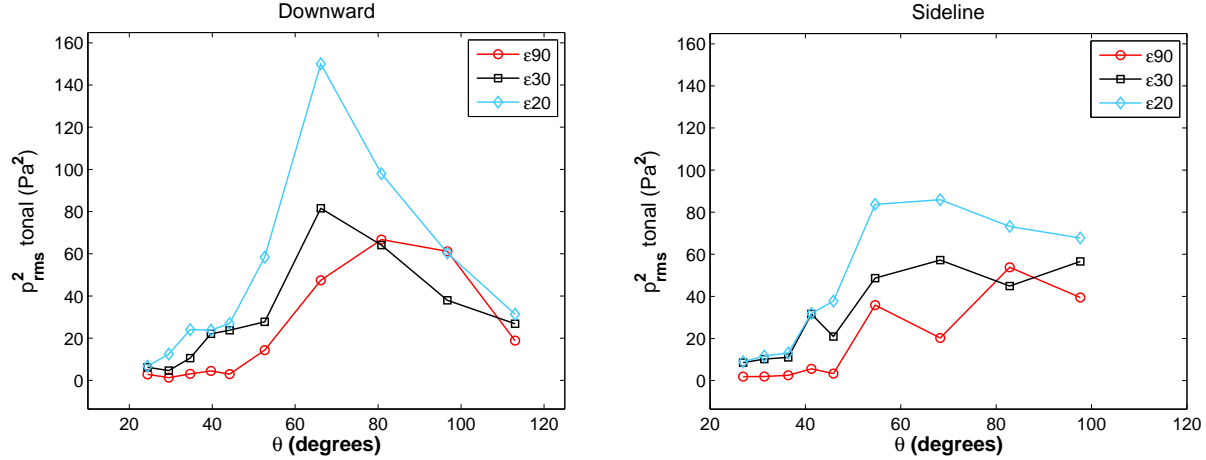


Figure 5.9: Tonal acoustic intensity for downward (left) and sideline (right) noise.

Although the downward and sideline noise in figure 5.9 were measured simultaneously, stark differences are seen in the two directions. This difference is believed to be caused by the strut hanging down from the ceiling, blocking and interfering the noise traveling in the sideline direction. From this point onwards, only the downward noise will be used in the analysis since it is believed to be less contaminated.

The  $\epsilon_{30}$  and  $\epsilon_{20}$  propellers appear to emit much larger amount of acoustic intensity in most directions compared to the  $\epsilon_{90}$  propeller. Very large differences (in %) are found in figure 5.10 for polar angles below  $80^\circ$ . This large increase in acoustic intensity was unexpected since the  $\epsilon_{30}$  and  $\epsilon_{20}$  propellers are identical to the  $\epsilon_{90}$  propeller in blade geometry and number.

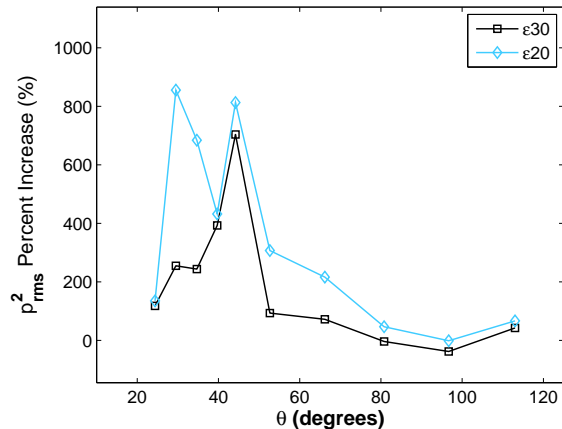


Figure 5.10: Percent difference in acoustic intensity from the  $\epsilon_{90}$  propeller.

Inspection of spectra at angles where the acoustic intensity increases were largest showed that large fractions of the total intensity were contained in the 0.5BPF tone (the spectra shown in figure 5.8 is a good example of this). 0.5BPF tones can often contain over 50% of the intensity of all the tones as shown in figure 5.11.

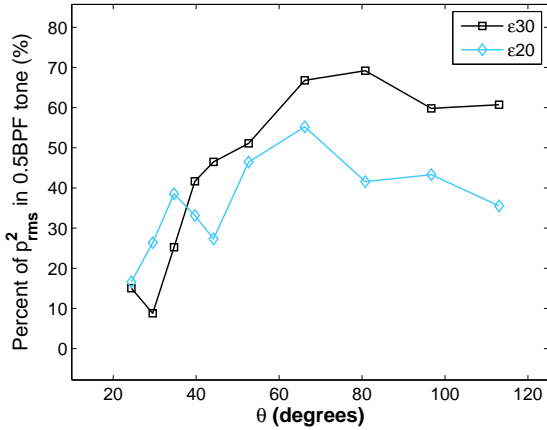


Figure 5.11: Percent of total acoustic intensity contained in the 0.5BPF tone.

If the intensity contained in the 0.5BPF tone is subtracted from the total intensity in figure 5.9, the result would be that shown in figure 5.12. With the 0.5BPF ignored, the tonal acoustic intensity in the  $\epsilon 30$  and  $\epsilon 20$  propellers decreases in almost every direction. The use of uneven blade spacing can cause the emission of far greater levels of tonal acoustic intensity, but the additional intensity is highly concentrated in the lowest frequency.

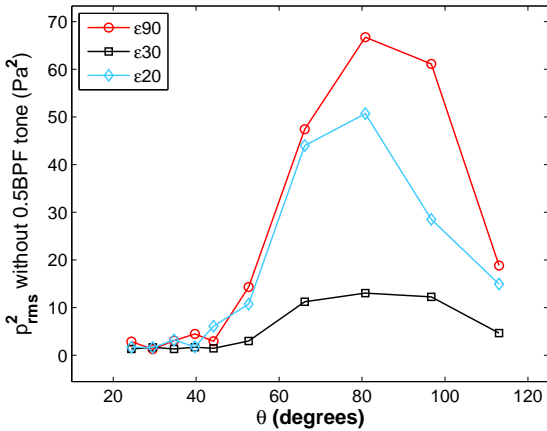


Figure 5.12: Total acoustic intensity without the 0.5BPF tone.

Because the 0.5BPF tone is at such a low frequency where the human ear is least sensitive, large amounts of sound at these frequencies can be “acceptable.” The degree to which the human ear’s sensitivity will play in this phenomena will be analyzed in the next section. But before moving on, some interesting trends are shown in figures 5.13 and 5.14. Figure 5.13 shows the changes in acoustic intensity of the “regular” tones (1BPF, 2BPF, 3BPF, ...) that are found in the  $\epsilon$ 90 propeller. The  $\epsilon$ 30 and  $\epsilon$ 20 propellers are found to have significant decreases in acoustic intensity contained in these “regular” tones compared to the  $\epsilon$ 90 propeller.

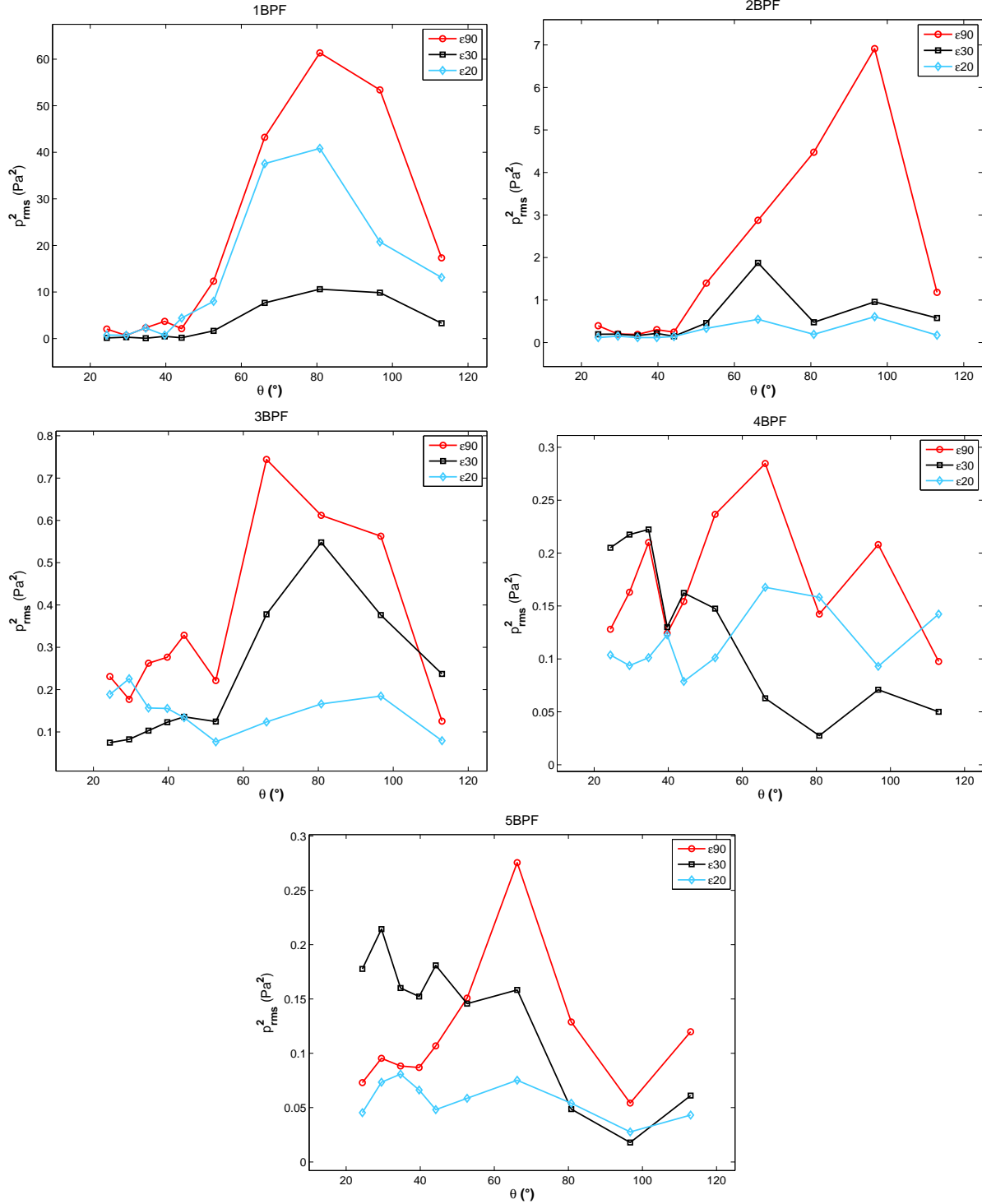


Figure 5.13: Changes in acoustic intensity in “regular tones.”

This decrease in intensity can be accounted for by the creation of the 0.5BPF, 1.5BPF, 2.5BPF, ... tones. The amount of intensity shifted into these tones are shown in figure 5.14.

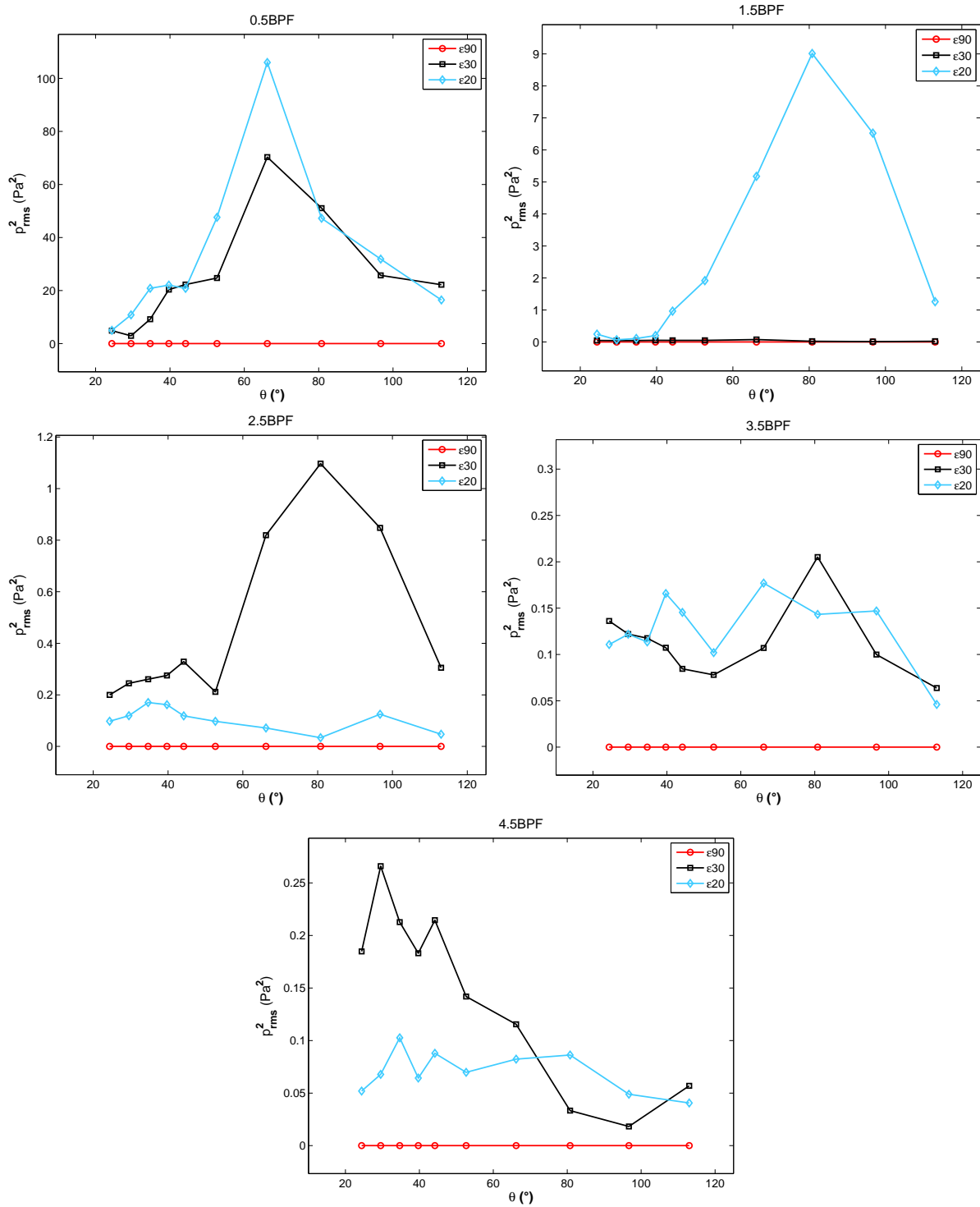


Figure 5.14: Shifting of acoustic intensity into “new” tones.

### 5.3 Overall Sound Pressure Level

The shift of acoustic intensity into the low frequency 0.5BPF tone is beneficial because the human ear is much less sensitive to low frequency sounds. A typical spectrum, with the first tone containing the most acoustic intensity is shown before and after A-weighting in figure 5.15. Because the 0.5BPF tone is of such a low frequency, the A-weighting tends to bring it far below the other tones.

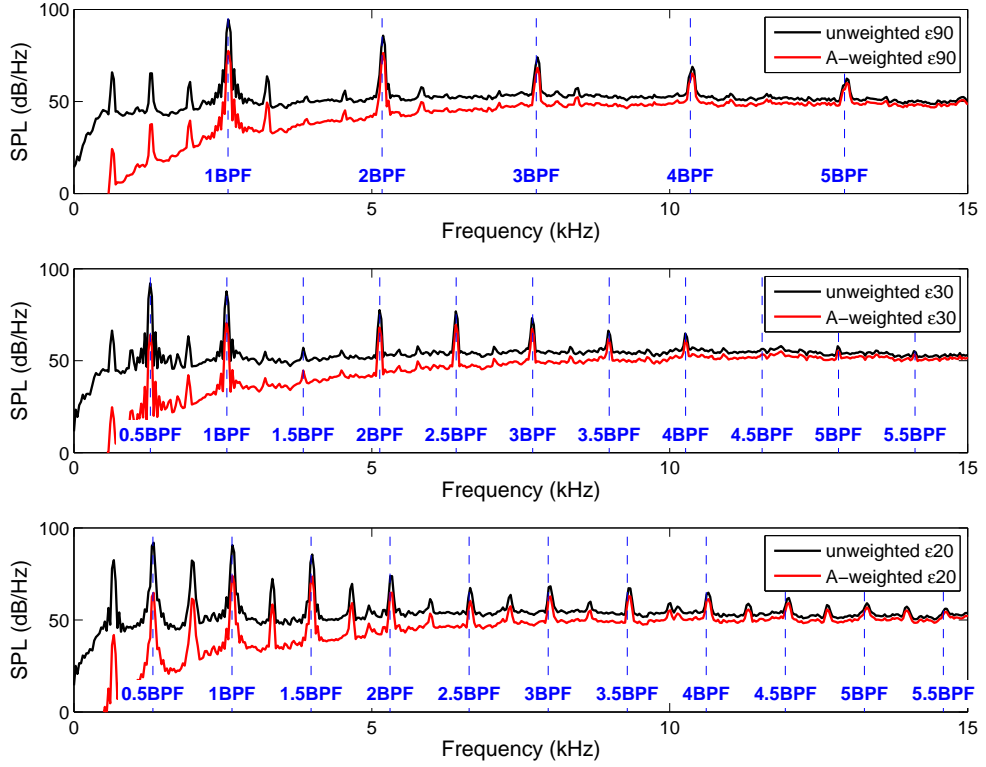


Figure 5.15: Unweighted and A-weighted spectra of  $\epsilon 90$  (top),  $\epsilon 30$  (middle), and  $\epsilon 20$  (bottom) at  $\theta = 96.7^\circ$ . A-weighting is performed after scaling the frequencies with the model scale factor.

The OASPL(A) for the tonal noise in all directions is shown in figure 5.16. The  $\epsilon 20$  and  $\epsilon 30$  propellers show reductions in OASPL(A) of up to 2 and 5 decibels respectively near the plane of the rotor ( $\theta = 90^\circ$ ). It is important to mention distortion of data due to thrust loss. Since the  $\epsilon 90$  propeller produced the most thrust, it is expected to create more tonal noise. How much this affects the OASPL(A) measurements is unknown.

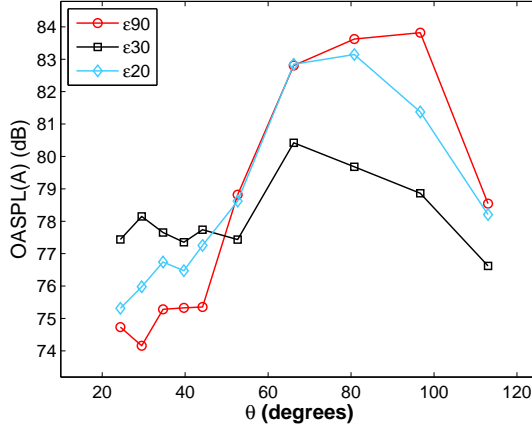


Figure 5.16: OASPL(A) of 0.5BPF through 5BPF tones.

The change in OASPL(A) is shown in figure 5.17. Figure 5.17 clearly shows that the reductions in tonal noise is concentrated near the plane of the propeller. For directions behind of the propeller ( $\theta$  approaching  $0^\circ$ ), tonal noise of the  $\epsilon 30$  and  $\epsilon 20$  propellers are found to be higher than that of the  $\epsilon 90$  propeller. Comparison to theory shows that experiments are in agreement with the general trend of decreasing OASPL(A) near  $\theta = 90^\circ$  and increasing OASPL(A) below  $\theta = 50^\circ$ . However, levels of OASPL(A) reductions for individual points often disagree with theory with relatively large errors.

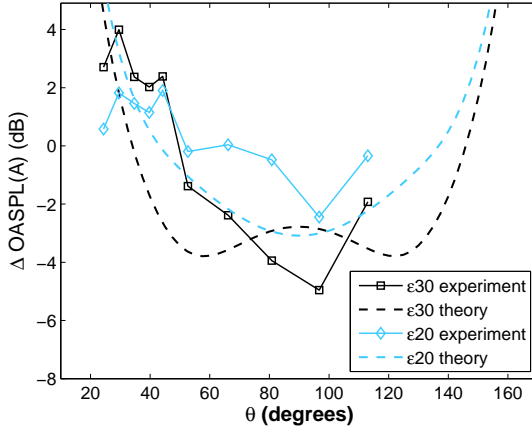


Figure 5.17: Change in OASPL(A) from the  $\epsilon 90$  propeller compared to theoretical predictions.

The results in figure 5.17 were calculated using tones 0.5BPF through 5BPF, which are the first five tones in the  $\epsilon 90$  propeller and the first ten tones for the  $\epsilon 30$  and  $\epsilon 20$  propellers. How-

ever, the  $\varepsilon_{30}$  and  $\varepsilon_{20}$  spectra often show an 11<sup>th</sup> tone, the 5.5BPF tone. The 5.5BPF tones are usually small, but because they appear at high frequencies, they can add a significant amount of A-weighted noise. The noise reduction calculations of figures 5.16 and 5.17 were redone with the addition of the 5.5BPF tone and are shown in figures 5.18 and 5.19. These tones appear to add no more than 1 decibel in any direction. However, it is still significant considering that it is coming from a single tone.

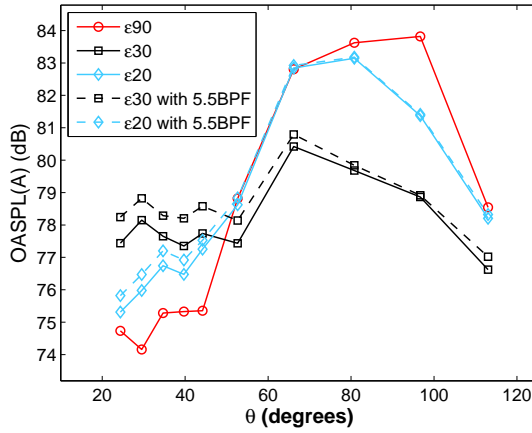


Figure 5.18: OASPL(A) from the  $\varepsilon_{90}$  propeller with the 5.5BPF tone.

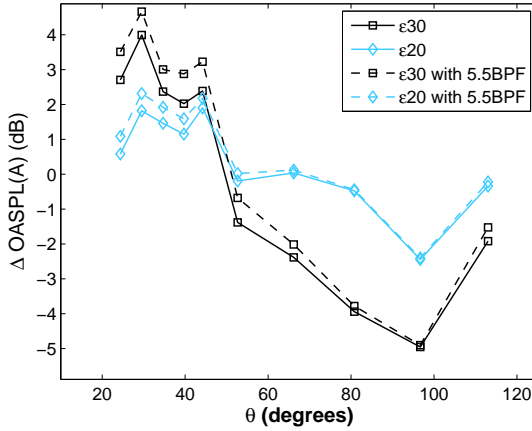


Figure 5.19: Change in OASPL(A) from the  $\varepsilon_{90}$  propeller with the 5.5BPF tone.

The OASPL(A) values in figures 5.16, 5.17, 5.18, and 5.19 were calculated after filtering out the broadband noise. For completeness, figure 5.20 shows the changes in OASPL(A) using the unfiltered spectra that includes both the tonal and broadband noise. Because of the unexpected

increase in broadband noise, the OASPL(A) for the  $\varepsilon 30$  and  $\varepsilon 20$  propellers is noticeably higher than before. The only reason that the  $\varepsilon 30$  and  $\varepsilon 20$  propellers are not any noisier than the  $\varepsilon 90$  propeller close to the plane of the propeller is that the rise in broadband noise is canceled out by the decrease in tonal noise. Again, the use of axial spacing between adjacent propeller blades should eliminate the increases in broadband noise.

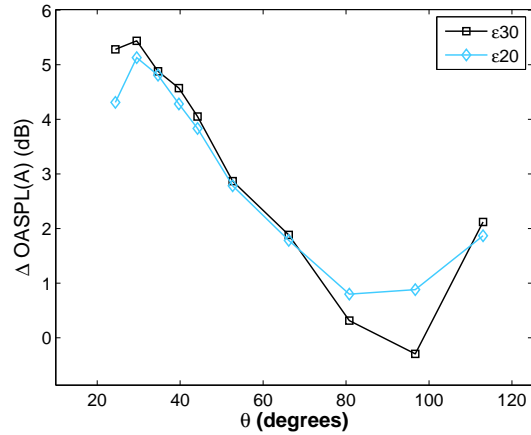


Figure 5.20: Changes in OASPL(A) from the  $\varepsilon 90$  propeller with both tonal and broadband noise.

# **Chapter 6**

## **Conclusion**

### **6.1 Summary**

An experimental study was conducted on the noise characteristics of four-bladed general aviation propellers with uneven blade spacing. The subscale propellers were initially designed using the geometry of the four-bladed McCauley propeller used on the Beechcraft King Air 350 series aircraft and later modified to increase the strength of the propellers. The 4-inch diameter (1:22.5 scale) subscale propellers were manufactured using high-resolution stereolithography and were powered by a high performance, radio controlled brushless electric motor. In general, these experiments have shown that it is possible to study propeller noise using 3D printed propellers. However, the plastic material is prone to failing under centrifugal and bending loads so they must be carefully designed to maximize structural strength.

Acoustic measurements were taken with a 24-microphone array housed inside an anechoic chamber for polar angles between  $20^\circ$  to  $120^\circ$ . The results showed significant increases in total acoustic intensity for propellers with uneven blade spacing, with very high concentrations of energy in the 0.5BPF tone. As predicted by the theory, the use of uneven blade spacing tends to shift tonal noise away from the plane of the propeller. Decreases in OASPL(A) of up to 5 dB were found near polar angles of  $90^\circ$  while increases of up to 4 dB were found for polar angles below  $50^\circ$ . This

is beneficial for noise metrics such as flyover noise, as noise at low polar angles are “weighted” less than noise near the plane of the propeller. Overall, the concept of uneven blade spacing has potential to reduce propeller tonal noise without adding excessive complexity to propeller design.

## 6.2 Recommendations for future work

Future work should prioritize meeting the similarity conditions. Due to the destruction of the  $\epsilon 30$  propeller, the target tip Mach number of 0.77 and disc loading of 0.23 psi were not reached. It is unknown whether or not the propeller blades would have been able to withstand the centrifugal and bending loads at 50,000 RPM, but the propellers would certainly not have reached the required disc loading due to a combination of the downwash effects described in section 5.1 as well as an over prediction of thrust by blade element momentum theory prior to applying the Betz condition for minimum energy loss.

Future propeller designs should also incorporate axial spacing between adjacent propeller blades. Acoustic measurements showed that the propellers with unevenly spaced blades suffered from increases in broadband noise significant enough to completely negate the reductions in tonal noise. The compound propeller experiments suggest that increases in broadband noise can be avoided by adding axial spacing between the adjacent blades. Axial spacing will also have the added benefit of making the blades more resistant to centrifugal loads, since the merging of blades decreases the blade section area over which centrifugal loads must be distributed.

Finally, future work should incorporate forward flight effects. The acoustic and disc loading results shown in this study were done in static conditions because of the limitations of the facilities used. Understanding the effects of various flight regimes such as cruise, takeoff, and landing on propeller noise will be required to fully understand the effects of uneven blade spacing on propeller noise.

# Bibliography

- [1] 3D Systems Corporation. *Accura 60 Plastic*, April 2006.
- [2] R. M. Aarts. A comparison of some loudness measures for loudspeaker listening tests. *The Journal of the Audio Engineering Society*, 40(3):142–146, 1992.
- [3] C. N. Adkins and R. H. Liebeck. Design of optimum propellers. *Journal of Propulsion and Power*, 10(5):676–683, 1994.
- [4] T. Aviation. King air 350i. "<http://beechcraft.txtav.com/en/king-air-350i>", 2016.
- [5] H. E. Bass, L. C. Sutherland, A. J. Zuckerwar, D. T. Blackstock, and D. M. Hester. Atmospheric absorption of sound: Further developments. *The Journal of the Acoustical Society of America*, 97, 1995.
- [6] M. Boltezar, M. Mesaric, and A. Kuhelj. The influence of uneven blade spacing on the spl and noise spectra radiated from radial fans. *Journal of Sound and Vibration*, 216:697–711, 1998.
- [7] A. Cattanei, R. Ghio, and A. Bongiovì. Reduction of the tonal noise annoyance of axial flow fans by means of optimal blade spacing. *Applied Acoustics*, 68:1323–1345, 2007.
- [8] W. Dobrzynski. Propeller noise reduction by means of unsymmetrical blade-spacing. *Journal of Sound and Vibration*, 163:123–136, December 1993.
- [9] M. Espayand and H. Lopez. The impact of airport noise and proximity on residential property values. *Growth and Change*, 31:408–419, 2000.
- [10] G. W. Evans, M. Bullinger, and S. Hygge. Chronic noise exposure and physiological response: A prospective study of children living under environmental stress. *Psychological Science*, 9:75–77, 1998.
- [11] D. Ewald, A. Pavlovic, and J. G. Bollinger. Noise reduction by applying modulation principles. *The Journal of the Acoustical Society of America*, 23:1381–1385, 1970.
- [12] Federal Aviation Administration. *Part 36, Noise Standards: Aircraft Type and Airworthiness Certification*, January 2002.
- [13] E. A. M. Franssen, C. M. A. G. van Wiechen, N. J. D. Nagelkerke, and E. Lebret. Aircraft noise around a large international airport and its impact on general health and medication use. *Occupational and Environmental Medicine*, 61:405–413, 2004.

- [14] R. Froude. On the part played in propulsion by differences of fluid pressure. *Transactions Institute Naval Architects*, 30:390, 1889.
- [15] D. B. Hanson. Helicoidal surface theory for harmonic noise of propellers in the far field. *AIAA*, 18:1213–1220, October 1980.
- [16] J. Lee and K. Nam. Development of low-noise cooling fan using uneven fan blade spacing. Technical Report SAE Technical Paper 2008-01-0569, Hyundai Motor Co., 2008.
- [17] G. Leishman. *Principles of Helicopter Aerodynamics*. Cambridge University Press, New York, 2 edition, 2002.
- [18] B. Maglione, D. Hanson, and R. Amiet. Aeroacoustics of flight vehicles: Theory and practice. Technical report, National Aeronautics and Space Administration, Langley Research Center, 1991.
- [19] J. E. Marte and D. W. Kurtz. A review of aerodynamic noise from propellers, rotors, and lift fans. Technical Report NASA-CR107568, National Aeronautics and Space Administration, Jet Propulsion Laboratory, 1970.
- [20] McCauley Propeller Systems. *STC Reference Manual*, May 2010.
- [21] R. C. Mellin and G. Sovran. Controlling the tonal characteristics of the aerodynamic noise generated by fan rotors. *Journal of Basic Engineering*, 92:143–154, 1970.
- [22] MonsterAutoParts.com. Nissan sentra radiator cooling fans, 2016.
- [23] A. Parry, M. Kingan, and B. Tester. Relative importance of open rotor tone and broadband noise sources. In *17th AIAA/CEAS Aeroacoustics Conference*, Portland, Oregon, 2011.
- [24] R. W. Paterson, P. G. Vogt, and M. R. Fink. Vortex noise on isolated airfoils. *Journal of Aircraft*, 10:296–302, 1973.
- [25] G. Pennington, N. Topham, and R. Ward. Aircraft noise and residential property values adjacent to manchester international airport. *Journal of Transport Economics and Policy*, 24:49–59, 1990.
- [26] V. C. Phong. Intermediate pressure bleed valve noise characterization and suppression. Master’s thesis, University of California, Irvine, 2011.
- [27] L. Prandtl and A. Betz. Screw propeller with minimum energy loss. *Gottinger Nachrichten*, pages 193–213, 1919.
- [28] W. Rankine. On the mechanical principles of the action of propellers. *Transactions Institute Naval Architects*, 6:13–39, 1865.
- [29] P. A. Shahady, C. A. Lyon, J. J. Schauer, M. H. Chopin, and M. S. Ewing. The effects of modulated blade spacing on static rotor acoustics and performance. *AIAA*, 73, 1973.

- [30] R. S. Shevell. *Fundamentals of Flight*. Prentice-Hall, Inc., Eaglewood Cliffs, New Jersey, 2 edition, 1989.
- [31] M. Smith. *Aircraft Noise*. Cambridge University Press, Cambridge, 1 edition, 1989.
- [32] S. A. Stansfeld and M. P. Matheson. Noise pollution: Non-auditory effects on health. *British Medical Bulletin*, 68:243–257, 2003.
- [33] A. D. Truong. Acoustic simulation of counter-rotating open rotor noise using very small scale model. Master’s thesis, University of California, Irvine, 2012.
- [34] T. Wright and W. E. Simmons. Blade sweep for low-speed axial fans. *Journal of Turbomachinery*, 112:151–158, January 1990.

## **Appendix A**

### **Blade Element Momentum Theory**

Designing the subscale propeller requires knowledge of how much thrust the subscale propeller will produce. The thrust must be known not only to match the disc loading of the McCauley propeller, but to ensure that the blades will not fail under the thrust load and to accurately model the propeller's acoustics. The well known blade element momentum theory (BEMT) is used to predict the forces on the propeller blades.

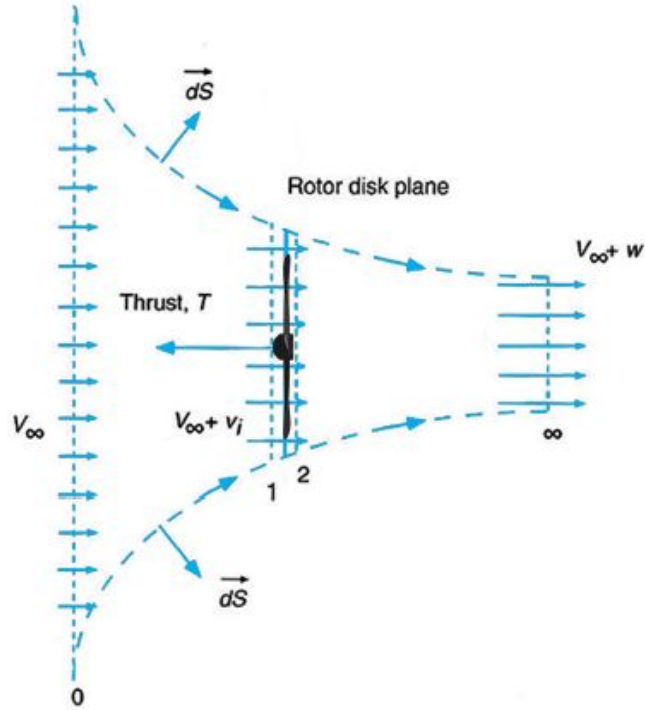


Figure A.1: Visualization of the streamtube around a propeller [17].

The momentum analysis was first done by Rankine and Froude in the analysis of marine propellers [28, 14]. The flow is visualized in figure A.1 and is assumed to be incompressible and isentropic everywhere except through the propeller disc. The conservation of total pressure in the isentropic regions are written as the following

$$P_0 + \frac{1}{2}\rho V_\infty^2 = P_1 + \frac{1}{2}\rho[V_\infty(1+a)]^2 \quad (\text{A.1})$$

$$P_0 + \frac{1}{2}\rho V_s^2 = P_2 + \frac{1}{2}\rho[V_\infty(1+a)]^2 \quad (\text{A.2})$$

Where  $a = \frac{v_i}{V_\infty}$  and  $V_s = V_\infty + w$ . Subtracting equation (A.1) from (A.2)

$$P_2 - P_1 = \frac{1}{2}\rho(V_s^2 - V_\infty^2) \quad (\text{A.3})$$

Assuming that the pressure is constant on either side of the propeller disc, the thrust produced by

the propeller is

$$T = (\Delta P)A = (P_2 - P_1)A \quad (\text{A.4})$$

Substituting equation (A.3) gives

$$T = \frac{1}{2}\rho(V_s^2 - V_\infty^2)A \quad (\text{A.5})$$

The differential thrust is therefore

$$dT = \frac{1}{2}\rho(V_s^2 - V_\infty^2)dA \quad (\text{A.6})$$

For a circular disc, this equation becomes

$$dT = \frac{1}{2}\rho(V_s^2 - V_\infty^2)2\pi r dr \quad (\text{A.7})$$

The thrust can also be calculated from the momentum deficit. The momentum of the fluid at the freestream condition and the slipstream condition are

$$\text{momentum in : } \rho V_\infty^2 A_\infty = (\rho V_\infty A_\infty) V_\infty = \dot{m} V_\infty \quad (\text{A.8})$$

$$\text{momentum out : } \rho V_s^2 A_s = (\rho V_s A_s) V_s = \dot{m} V_s \quad (\text{A.9})$$

The thrust is the difference between equations (A.8) and (A.9)

$$T = \dot{m}(V_s - V_\infty) \quad (\text{A.10})$$

The differential thrust from this equation is

$$dT = d\dot{m}(V_s - V_\infty) = \rho(2\pi r dr)V_\infty(1 + a)(V_s - V_\infty) \quad (\text{A.11})$$

Setting equations (A.7) and (A.11) equal to each other and canceling out like terms gives

$$V_\infty(1+a) = \frac{1}{2}(V_\infty + V_s) \quad (\text{A.12})$$

Substituting equation (A.14) into equation (A.7) for  $V_s$  and simplifying gives

$$dT = 4\rho a V_\infty^2 (1+a) \pi r dr \quad (\text{A.13})$$

$$dT = 4F\rho a V_\infty^2 (1+a) \pi r dr \quad (\text{A.14})$$

Where  $F$  is a function that corrects for the losses at the blade tip proposed by Prandtl [27].  $F$  has the form

$$F = \frac{2}{\pi} \arccos(\exp(-\frac{B}{2} \frac{1-\bar{r}}{\sin(\delta + \alpha_i)})) \quad (\text{A.15})$$

$$f = \frac{B}{2} \frac{1-\bar{r}}{\sin(\delta + \alpha_i)} \quad (\text{A.16})$$

Applying the Betz condition for minimum energy loss [3], the expression for  $f$  becomes

$$f = \frac{B}{2} \frac{1-\bar{r}}{\sin(\delta_{tip})} \quad (\text{A.17})$$

Where  $\delta_{tip}$  is the value of  $\delta$  at the blade tip (the induced angle of attack  $\alpha_i$  is zero at the tip). The only unknown in equation (A.14) is the inflow factor  $a$ . The inflow factor can be calculated from the analysis of a blade element.

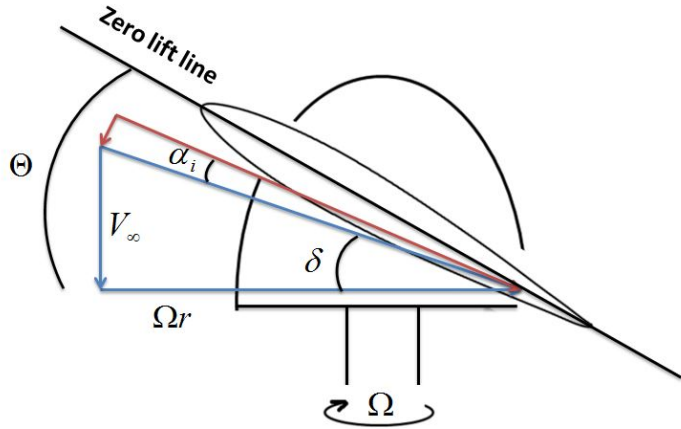


Figure A.2: Diagram of blade section.

From the geometry of the blade element with respect to the incoming flow, the differential thrust from a single blade is

$$dT = dL \cos(\delta + \alpha_i) - dD \sin(\delta + \alpha_i) \quad (\text{A.18})$$

Multiplying by the number of blades  $B$ , and ignoring the drag and induced angle of attack  $\alpha_i$  terms since they are small compared to the lift and angle of attack  $\delta$  respectively gives

$$dT = BdL \cos \delta = B \frac{1}{2} \rho (V_\infty^2 + \Omega^2 r^2) c_{l\alpha} (\Theta - \delta - \alpha_i) cdr \cos \delta \quad (\text{A.19})$$

Equating equation (A.19) to equation (A.14) and simplifying gives

$$B(V_\infty^2 + \Omega^2 r^2) c_{l\alpha} (\Theta - \delta - \alpha_i) c \cos \delta = 8FV_\infty^2 a(1+a)\pi r \quad (\text{A.20})$$

From the geometry, it can be shown that

$$\tan \alpha_i = \frac{v_i}{\sqrt{V_\infty^2 + \Omega^2 r^2}} \quad (\text{A.21})$$

Using small angle approximation,

$$v_i = \alpha_i \sqrt{V_\infty^2 + \Omega^2 r^2} \quad (\text{A.22})$$

Equating the axial induced velocities from the blade element and momentum analysis gives

$$aU_\infty = v_i \cos \delta \quad (\text{A.23})$$

Therefore

$$a = \frac{v_i \cos \delta}{V_\infty} = \frac{\alpha_i \sqrt{V_\infty^2 + \Omega^2 r^2} \cos \delta}{V_\infty} \quad (\text{A.24})$$

Substituting equation (A.24) into equation (A.20) and substituting for dimensionless variables:

$$\bar{V}_R = \frac{\sqrt{U_\infty^2 + \Omega^2 r^2}}{\Omega R}, \lambda = \frac{V_\infty}{\Omega R}, \sigma = \frac{Bc}{\pi R}, \bar{r} = \frac{r}{R}$$

$$\alpha_i^2 + \left[ \frac{\lambda}{\bar{r}} + \frac{\sigma c_{l\alpha} \bar{V}_R}{8F\bar{r}^2} \right] \alpha_i - \frac{\sigma c_{l\alpha} \bar{V}_R}{8F\bar{r}^2} (\Theta - \delta) = 0 \quad (\text{A.25})$$

Solving this quadratic equation for the positive root gives

$$\alpha_i = -\frac{1}{2} \left[ \frac{\lambda}{\bar{r}} + \frac{\sigma c_{l\alpha} \bar{V}_R}{8F\bar{r}^2} \right] + \sqrt{\frac{1}{4} \left[ \frac{\lambda}{\bar{r}} + \frac{\sigma c_{l\alpha} \bar{V}_R}{8F\bar{r}^2} \right]^2 + \frac{\sigma c_{l\alpha} \bar{V}_R}{8F\bar{r}^2} (\Theta - \delta)} \quad (\text{A.26})$$

Equation (A.26) shows that the induced angle of attack  $\alpha_i$  is a function of  $\alpha_i$  (since  $F$  is a function of  $\alpha_i$ ). So equation (A.26) is iterated until the value for  $\alpha_i$  converges. Once  $\alpha_i$  is known, equation (A.19) can be used to calculate the differential thrust.

# Appendix B

## Stress Analysis

There are two main sources of stress on a propeller blade. The first is the centripetal force, which is applied in the radial direction as the propeller spins. The second is thrust distribution across the blade, which is applied axially.

The vast majority of stresses applied to propeller blades are due to centripetal forces from the rotation of the propeller blades. A simplified method of estimating stresses due to centripetal forces is crucial in designing propellers for structural integrity. The centripetal force at any point on the blade is described by

$$F_c = \frac{mv^2}{r} = m\Omega^2 r \quad (\text{B.1})$$

However, the radial coordinate ( $r$ ) and the mass ( $m$ ) supported at each radial coordinate varies along the propeller blade. So the blade is divided into  $n$  radial segments (blade sections) and the centripetal force is calculated at each blade section.

$$F_c(r) = \Omega^2 r_n \sum_{n=1}^n m_n \quad (\text{B.2})$$

The centripetal force at each blade section is divided by the blade cross sectional area ( $A$ ) to find the stress due to centripetal force ( $\sigma_c$ ) at each blade section. The area of the blade section will be

discussed in the thrust contribution section.

$$\sigma_c(r) = F_c(r)/A(r) \quad (\text{B.3})$$

While the centripetal force acts radially and wants to pull the blade apart, the thrust force acts axially and wants to bend the blade. This bending is modeled using Euler-Bernoulli beam theory. To apply this beam theory, the propeller blade is simplified as a constant chord, straight blade with no twist. The worst case scenario is applied by using the smallest geometric angle of attack found in the real propeller blade.

Prior to applying the beam theory, a method of calculating the blade section area, centroid locations ( $c_y, c_z$ ), and the second moment of inertias ( $I_y, I_z, I_{yz}$ ). Figure B.1 shows a blade cross section. The complex geometry of the airfoil shape can be converted into a polygon by connecting points along the upper and lower surfaces of the airfoil.

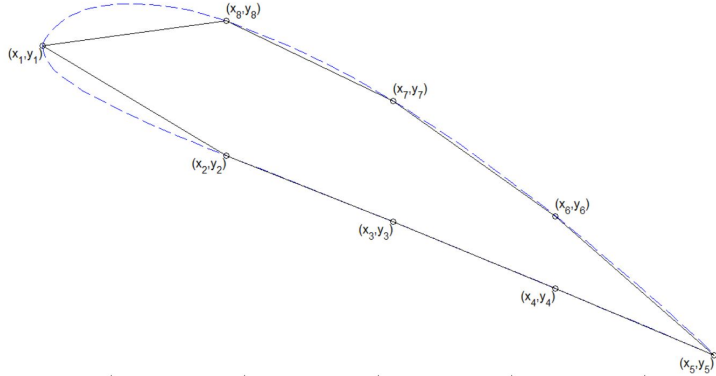


Figure B.1: Polygon Method. Only 8 vertices are shown for simplicity. More vertices are required to more accurately represent the airfoil using a polygon.

The area, centroid, and moment of inertias of a polygon can be found using the vertices of

the polygon by the following equations (index  $i = N + 1$  refers to the  $i = 1$ ):

$$\begin{aligned}
A &= \frac{1}{2} \sum_{i=1}^N (y_i z_{i+1} - y_{i+1} z_i) \\
c_y &= \frac{1}{6A} \sum_{i=1}^N (y_i + y_{i+1})(y_i z_{i+1} - y_{i+1} z_i) \\
c_z &= \frac{1}{6A} \sum_{i=1}^N (z_i + z_{i+1})(y_i z_{i+1} - y_{i+1} z_i) \\
I_y &= \frac{1}{12} \sum_{i=1}^N (z_i^2 + z_i z_{i+1} + z_{i+1}^2)(y_i z_{i+1} - y_{i+1} z_i) \\
I_z &= \frac{1}{12} \sum_{i=1}^N (y_i^2 + y_i y_{i+1} + y_{i+1}^2)(y_i z_{i+1} - y_{i+1} z_i) \\
I_{yz} &= \frac{1}{12} \sum_{i=1}^N (y_i z_{i+1} + 2y_i z_i + 2y_{i+1} z_{i+1} + y_{i+1} z_i)(y_i z_{i+1} - y_{i+1} z_i)
\end{aligned} \tag{B.4}$$

These equations can be applied to each blade section to find the radial distributions of area, centroid locations, and the second moment of inertias. These distributions must be known to solve the Euler-Bernoulli beam equation.

The Euler-Bernoulli beam bending theory states that the beam deflection ( $w$ ) is related to the Young's Modulus ( $E$ ), second moment of inertia ( $I$ ), and axial load distribution ( $T$ ) by the following fourth-order differential equation:

$$\frac{d^2}{dx^2}(EI \frac{d^2 w}{dx^2}) = T(x) \tag{B.5}$$

If the beam is initially straight, maintains the same cross section throughout the beam, and has homogeneous material properties, equation (B.5) can be simplified into equation (B.6), where  $E$  and  $I$  are constants.

$$EI \frac{d^4 w}{dx^4} = T(x) \tag{B.6}$$

The bending moment of the beam can be expressed in terms of the beam deflection and is given by

$$M(x) = -EI \frac{d^2 w}{dx^2} \tag{B.7}$$

Combining equations (B.6) and (B.7) gives the following expression for the bending moment

$$M(x) = -EI \int \int \frac{1}{EI} T(x) dx \quad (\text{B.8})$$

$T(x)$  is the axial load distribution on the beam, which in this case, is the thrust distribution along the blade found from Blade Element Momentum theory. Solving equation (B.8) for a real propeller with varying chord lengths and twist along the blade is difficult as  $E$  and  $I$  are not constant. To simplify the analysis, the bending moment  $M$  is found for a simple propeller blade with constant chord length and no twist. To simulate the worst case scenario, the simplified propeller blade has the chord length and geometric angle of attack found at tip cross section of the real propeller. With this simplification, equation (B.8) simplifies into equation (B.9) and can be easily integrated.

$$M(x) = - \int \int T(x) dx \quad (\text{B.9})$$

In general, the stress at any point in the beam cross section at a specific  $x$ -coordinate value is

$$\sigma_x(y, z) = -\frac{M_z I_y + M_y I_{yz}}{I_y I_z - I_{yz}^2} (y - c_y) + \frac{M_y I_z + M_z I_{yz}}{I_y I_z - I_{yz}^2} (z - c_z) \quad (\text{B.10})$$

In equation B.10, the second moment of inertias vary along  $x$  as the propeller blade twists and varies in chord length. It is important to note that the stress due to the thrust distribution is a function of  $x$ ,  $y$ , and  $z$  while the stress due to the centripetal force is only a function of  $x$ . Adding the two stresses at each point in the propeller blade gives the total stress.

The bending moment causes the highest amounts of stress when the values  $y - c_y$  and  $z - c_z$  are maximized. Therefore, the maximum stress will be found along the edge of the blade cross section, or along the surface of the propeller blade.

## Appendix C

### Unweighted vs. A-weighted Spectra

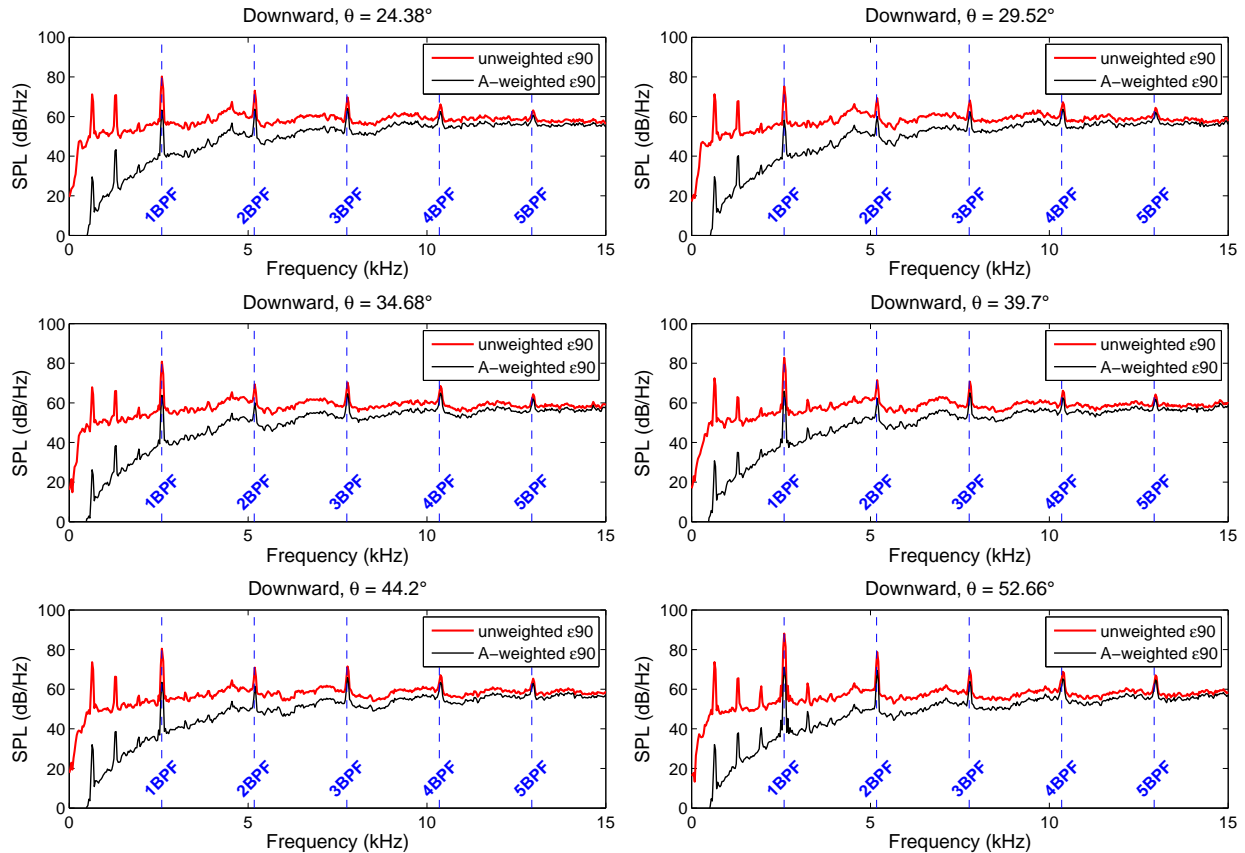


Figure C.1: Unweighted vs. A-weighted spectra of the  $\epsilon 90$  propeller.

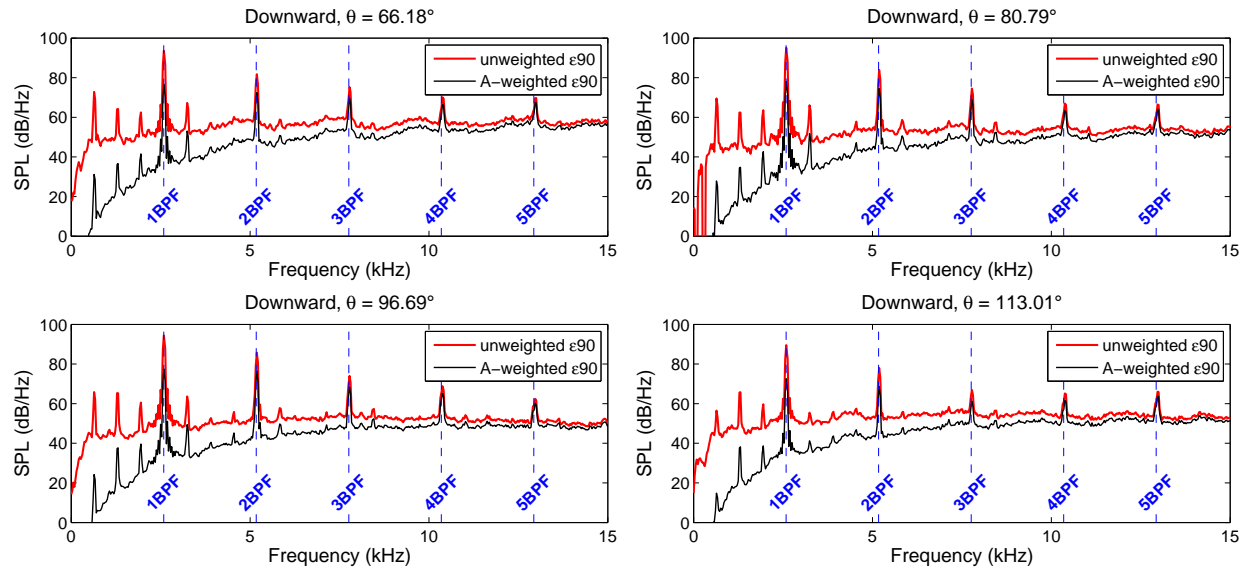


Figure C.2: Unweighted vs. A-weighted spectra of the  $\epsilon 90$  propeller (continued).

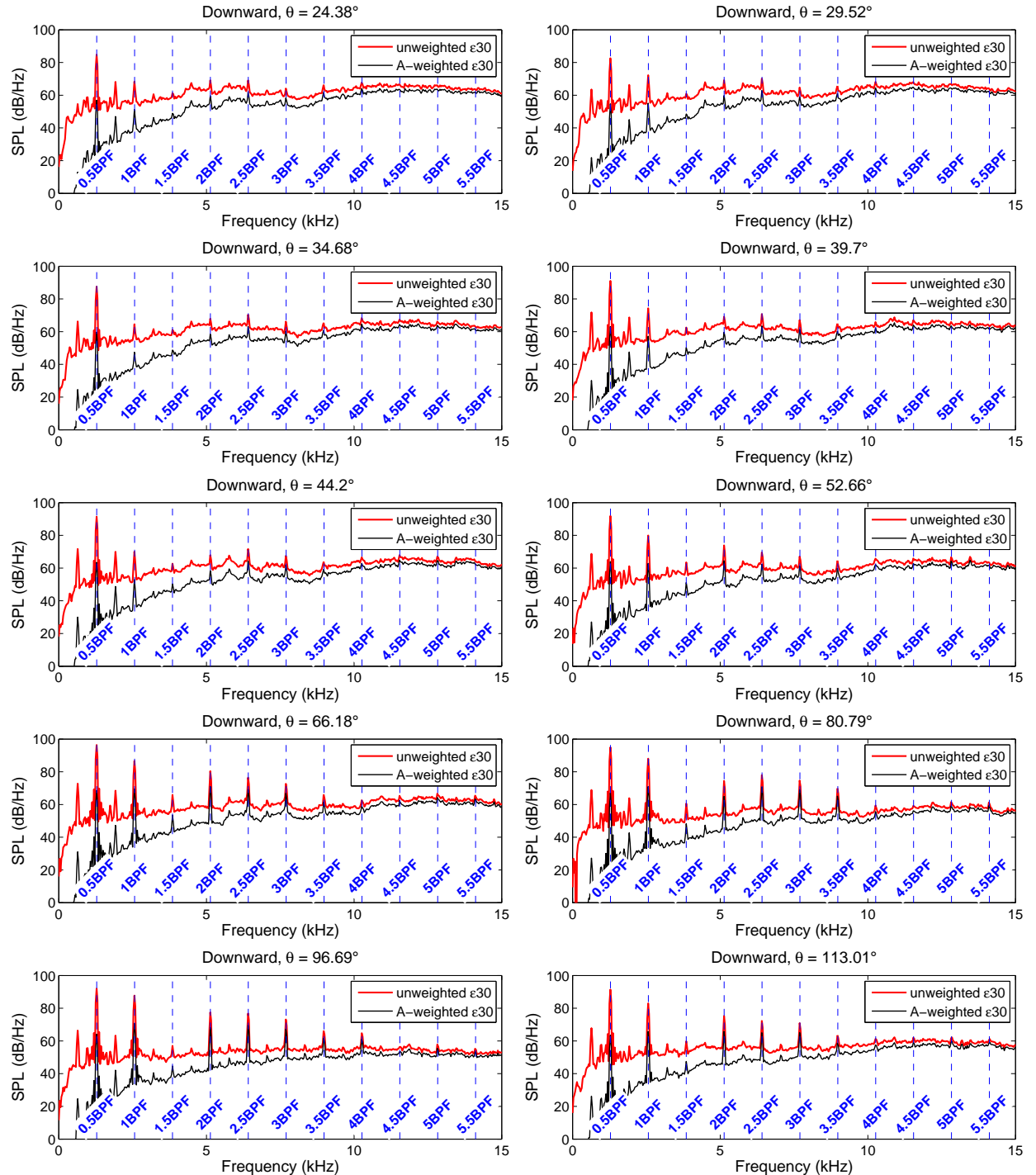


Figure C.3: Unweighted vs. A-weighted spectra of the  $\epsilon 30$  propeller.

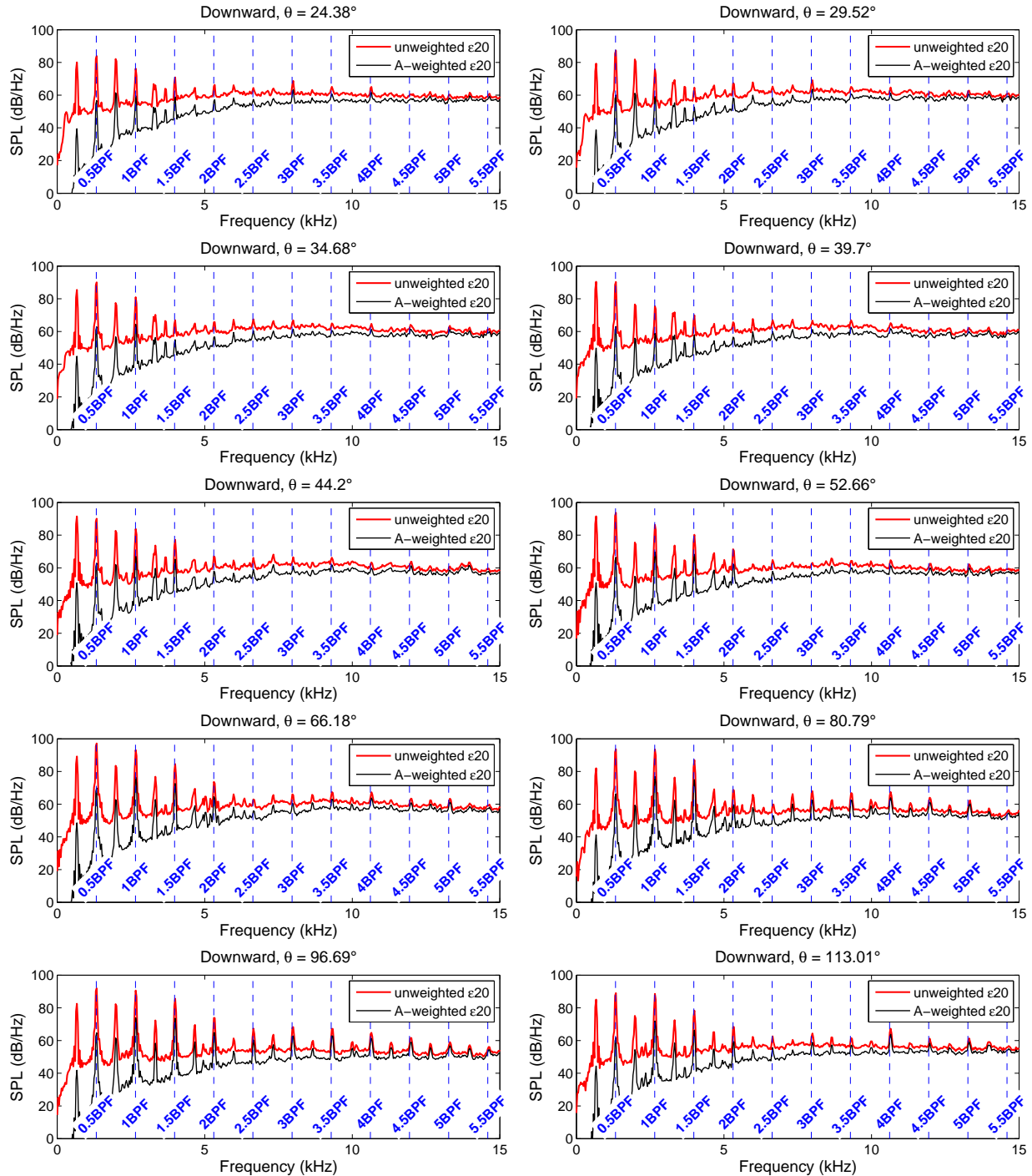


Figure C.4: Unweighted vs. A-weighted spectra of the  $\epsilon 20$  propeller.

## Appendix D

### Unweighted Spectra

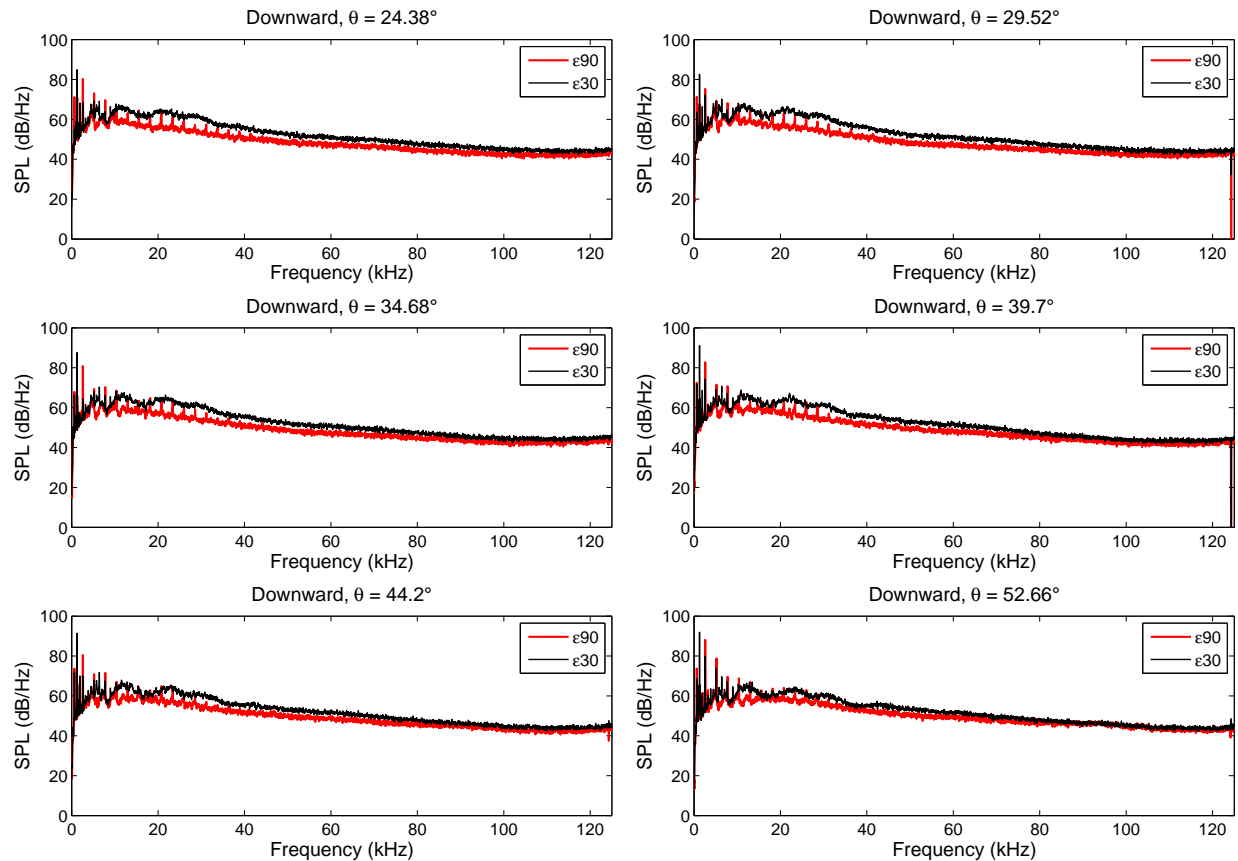


Figure D.1:  $\epsilon_{90}$  vs  $\epsilon_{30}$  unweighted Spectra.

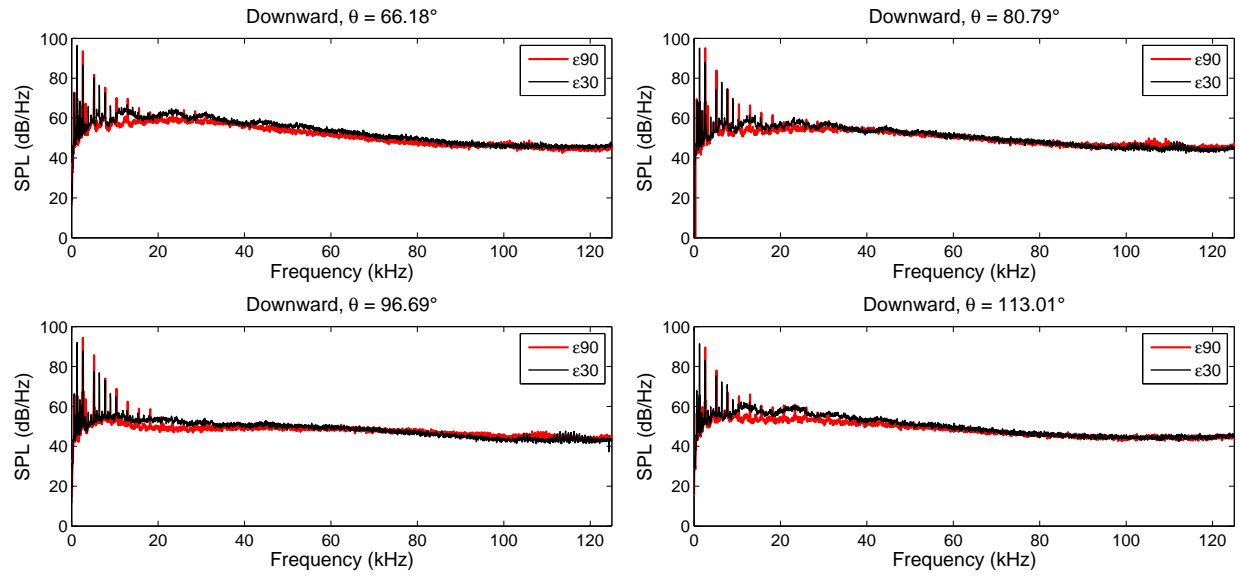


Figure D.2:  $\epsilon 90$  vs  $\epsilon 30$  unweighted Spectra (continued).

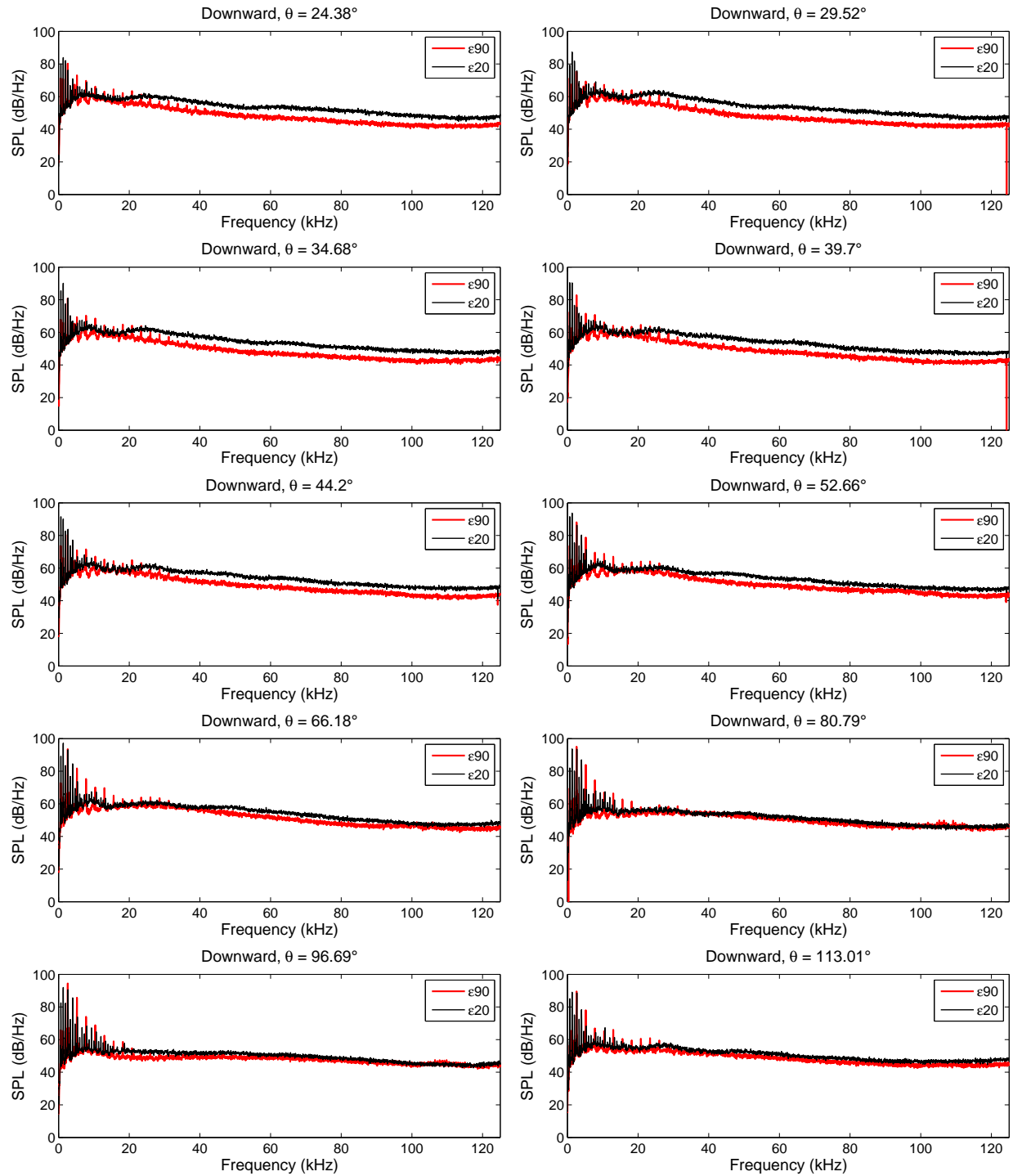


Figure D.3:  $\epsilon_{90}$  vs  $\epsilon_{20}$  unweighted Spectra.

## Appendix E

# Unweighted Spectra, Compound Propellers

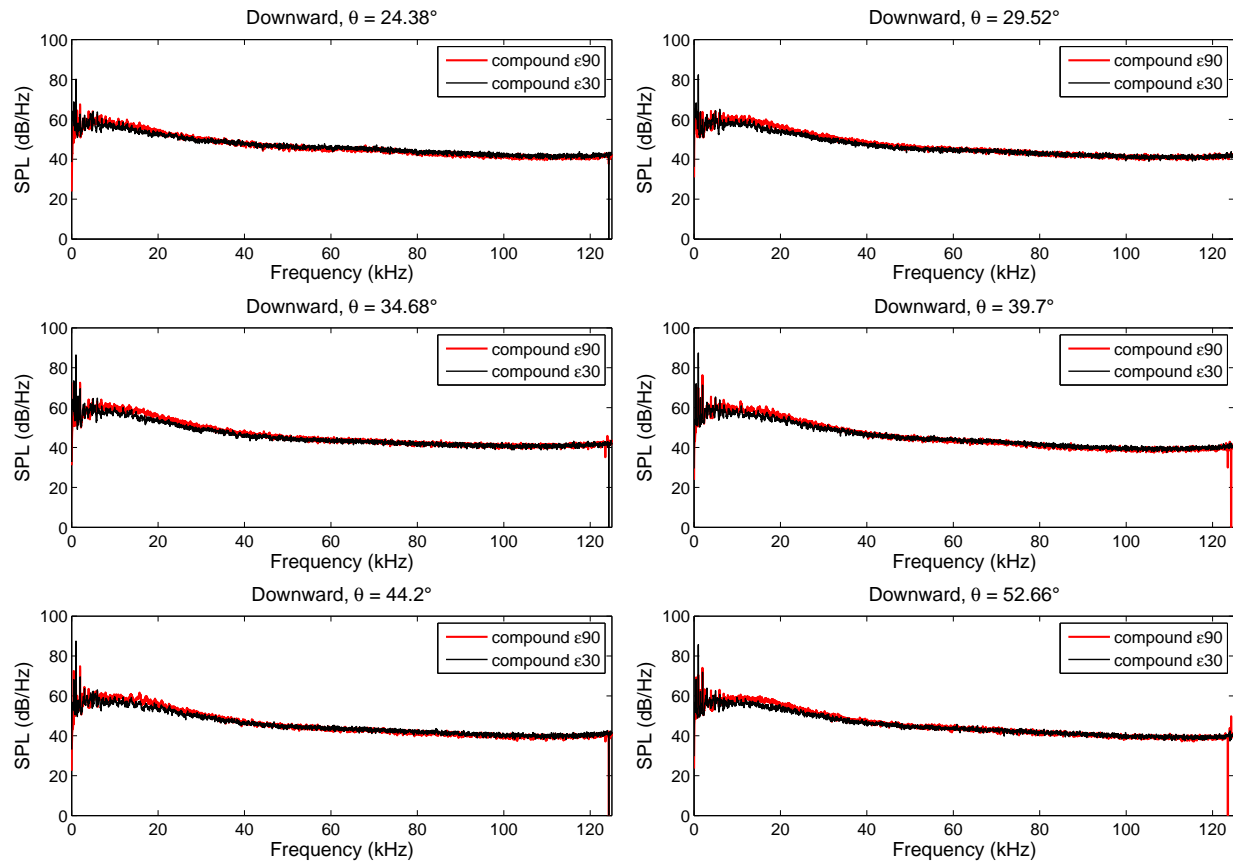


Figure E.1: Compound  $\epsilon 90$  vs compound  $\epsilon 30$  unweighted Spectra.

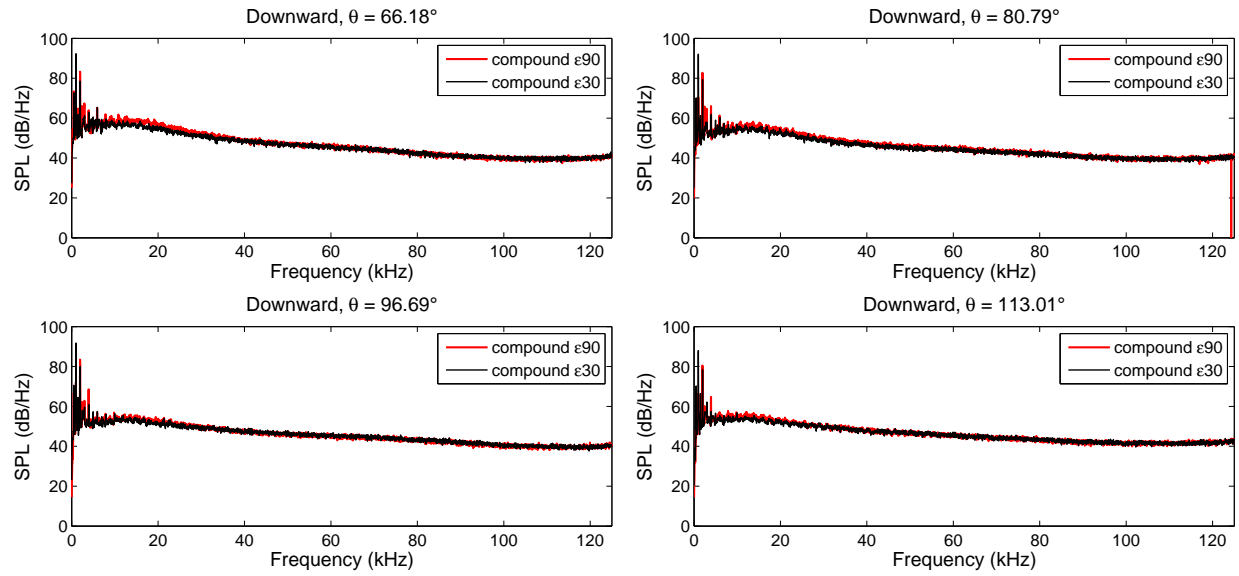


Figure E.2: Compound  $\epsilon 90$  vs compound  $\epsilon 30$  unweighted Spectra (continued).

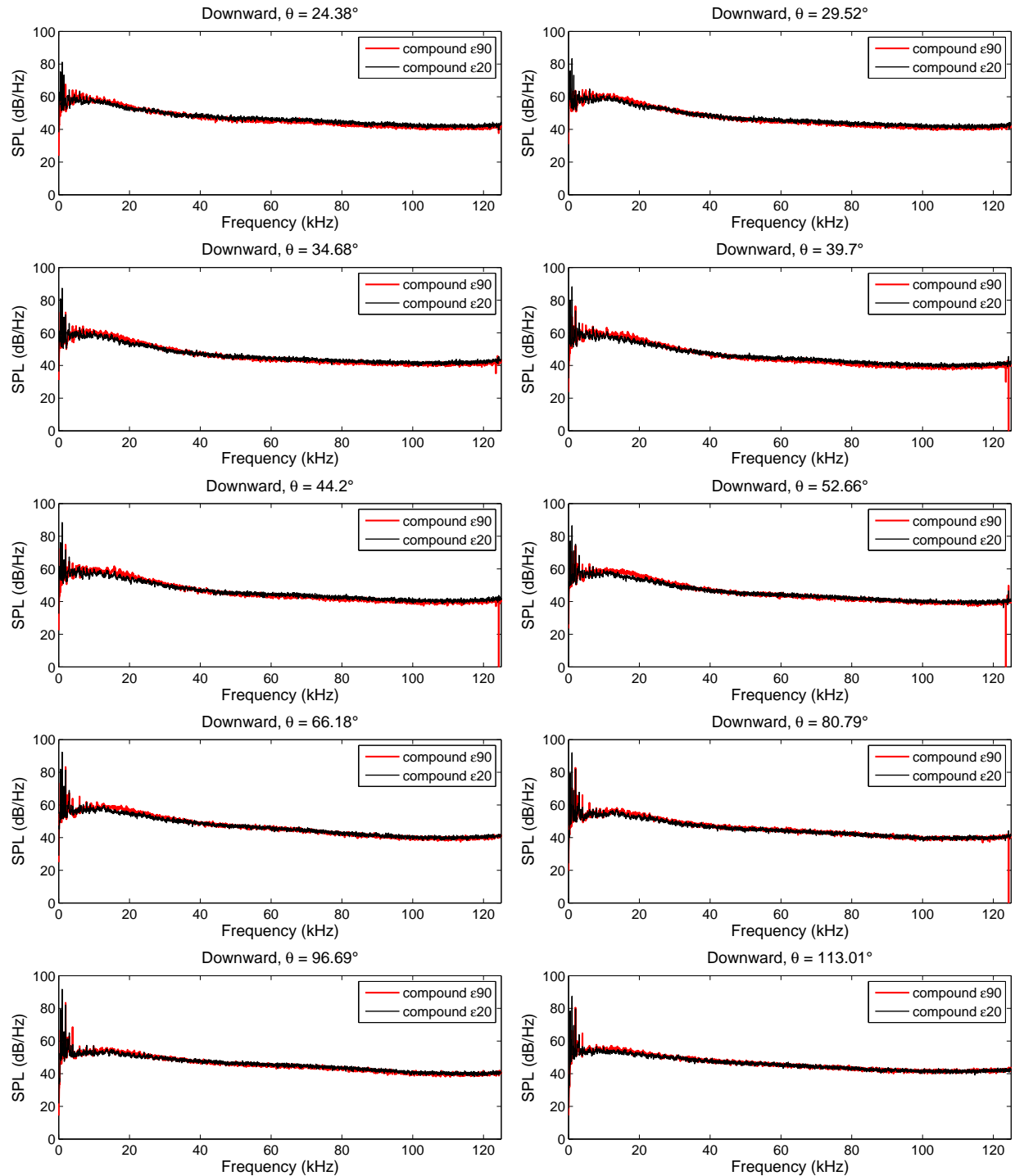


Figure E.3: Compound  $\epsilon 90$  vs compound  $\epsilon 20$  unweighted Spectra.